Cell

Article

The bone microenvironment invigorates metastatic seeds for further dissemination

Graphical abstract

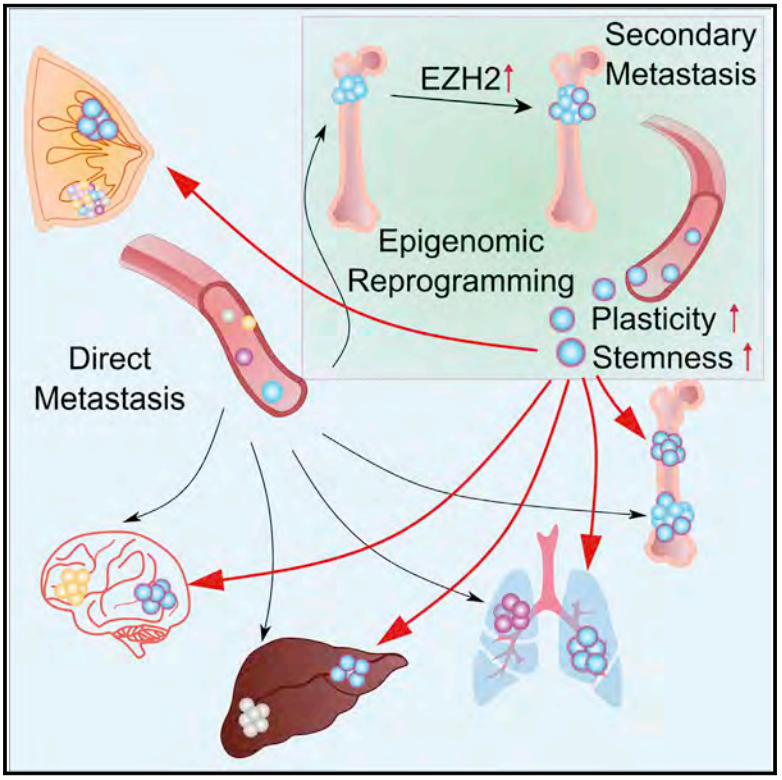

Highlights

- Experimental bone metastases (BoM) spread to other organs in mouse models
- Evolving barcodes delineate further spread from BoM in spontaneous metastasis
- BoM spurs metastatic seeds with increased stemness and reduced organotropism
- EZH2 mediates secondary metastasis invigorated by the bone microenvironment

Authors

Weijie Zhang, Igor L. Bado, Jingyuan Hu, ..., Chonghui Cheng, Zhandong Liu, Xiang H.-F. Zhang

Correspondence

xiangz@bcm.edu

In brief

Delineation of cancer cell spreading from primary bone metastasis by an evolving barcode system highlights the impact of the bone microenvironment in shaping secondary metastasis through mechanisms distinct from clonal selection.

Zhang et al., 2021, Cell *184*, 2471–2486
April 29, 2021
https://doi.org/10.1016/j.cell.2021.03.011

CellPress

Cell

CellPress

Article

The bone microenvironment invigorates metastatic seeds for further dissemination

Weijie Zhang,[1,2,3,11] Igor L. Bado,[1,2,3,11] Jingyuan Hu,[4,5] Ying-Wooi Wan,[4,6] Ling Wu,[1,2,3] Hai Wang,[1,2,3] Yang Gao,[1,2,3] Hyun-Hwan Jeong,[4,6] Zhan Xu,[1,2,3] Xiaoxin Hao,[1,2,3] Bree M. Lege,[1,6] Rami Al-Ouran,[4,7] Lucian Li,[4,7] Jiasong Li,[8] Liqun Yu,[1,2,3] Swarnima Singh,[1,2,3] Hin Ching Lo,[1,2,3] Muchun Niu,[9] Jun Liu,[1,2,3] Weiyu Jiang,[1,2,3] Yi Li,[1,2,3] Stephen T.C. Wong,[2,3,8] Chonghui Cheng,[1,6] Zhandong Liu,[4,6] and Xiang H.-F. Zhang[1,2,3,10,12,*]

[1]Lester and Sue Smith Breast Center, Baylor College of Medicine, Houston, TX 77030, USA
[2]Dan L. Duncan Cancer Center, Baylor College of Medicine, Houston, TX 77030, USA
[3]Department of Molecular and Cellular Biology, Baylor College of Medicine, Houston, TX 77030, USA
[4]Jan and Dan Duncan Neurological Research Institute, Texas Children's Hospital, Houston, TX 77030, USA
[5]Quantitative and Computational Biosciences Program, Baylor College of Medicine, Houston, TX 77030, USA
[6]Department of Molecular and Human Genetics, Baylor College of Medicine, Houston, TX 77030, USA
[7]Department of Pediatrics, Baylor College of Medicine, Houston, TX 77030, USA
[8]Department of Systems Medicine and Bioengineering and Translational Biophotonics Laboratory, Houston Methodist Cancer Center, Houston, TX 77030, USA
[9]Integrative Molecular and Biomedical Sciences Graduate Program, Baylor College of Medicine, Houston, TX 77030, USA
[10]McNair Medical Institute, Baylor College of Medicine, Houston, TX 77030, USA
[11]These authors contributed equally
[12]Lead contact
*Correspondence: xiangz@bcm.edu
https://doi.org/10.1016/j.cell.2021.03.011

SUMMARY

Metastasis has been considered as the terminal step of tumor progression. However, recent genomic studies suggest that many metastases are initiated by further spread of other metastases. Nevertheless, the corresponding pre-clinical models are lacking, and underlying mechanisms are elusive. Using several approaches, including parabiosis and an evolving barcode system, we demonstrated that the bone microenvironment facilitates breast and prostate cancer cells to further metastasize and establish multi-organ secondary metastases. We uncovered that this metastasis-promoting effect is driven by epigenetic reprogramming that confers stem cell-like properties on cancer cells disseminated from bone lesions. Furthermore, we discovered that enhanced EZH2 activity mediates the increased stemness and metastasis capacity. The same findings also apply to single cell-derived populations, indicating mechanisms distinct from clonal selection. Taken together, our work revealed an unappreciated role of the bone microenvironment in metastasis evolution and elucidated an epigenomic reprogramming process driving terminal-stage, multi-organ metastases.

INTRODUCTION

Metastasis to distant organs is the major cause of cancer-related deaths. Bone is the most frequent destination of metastasis in breast cancer and prostate cancer (Gundem et al., 2015; Kennecke et al., 2010; Smid et al., 2008). In the advanced stage, bone metastasis is driven by the paracrine crosstalk among cancer cells, osteoblasts, and osteoclasts, which together constitute an osteolytic vicious cycle (Esposito et al., 2018; Kang et al., 2003; Kingsley et al., 2007; Weilbaecher et al., 2011). Specifically, cancer cells secrete molecules such as PTHrP, which act on osteoblasts to modulate the expression of genes including RANKL and OPG (Boyce et al., 1999; Juárez and Guise, 2011). The alterations of these factors, in turn, boost osteoclast maturation and accelerate bone resorption. Many growth factors (e.g., IGF1) deposited in the bone matrix are then released and reciprocally stimulate tumor growth. This knowledge laid the foundation for clinical management of bone metastases (Coleman et al., 2008).

The urgency of bone metastasis research is somewhat controversial. It has long been noticed that, at the terminal stage, breast cancer patients usually die of metastases in multiple organs. In fact, compared to metastases in other organs, bone metastases are relatively easier to manage. Patients with the skeleton as the only site of metastasis usually have better prognosis than those with visceral organs affected (Coleman and Rubens, 1987; Coleman et al., 1998). These facts argue that perhaps metastases in more vital organs should be prioritized in research. However,

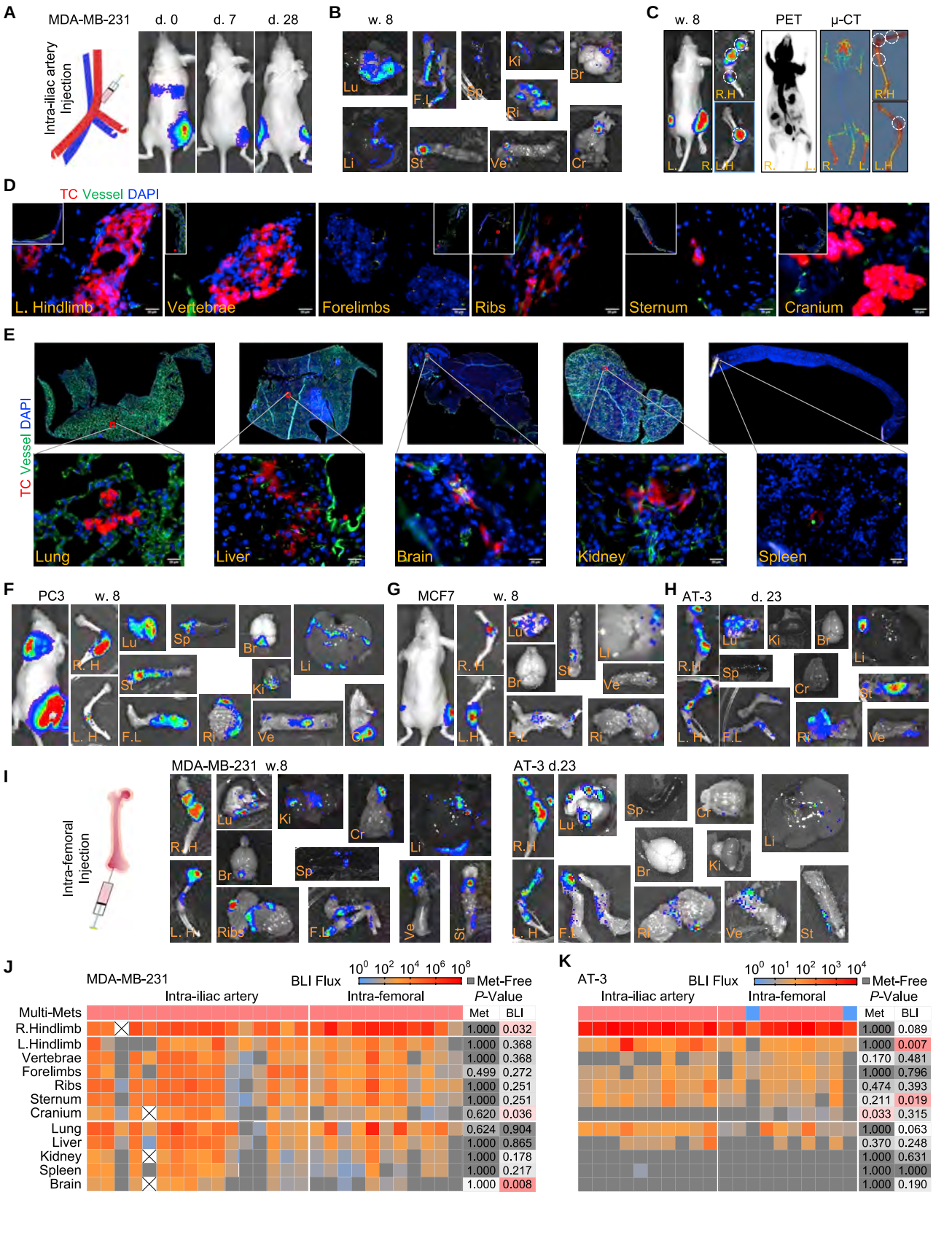

(legend on next page)

metastases usually do not occur synchronously. In 45% of metastatic breast cancer cases, bone is the first organ that shows signs of metastasis, much more frequently compared to the lungs (19%), liver (5%), and brain (2%) (Coleman and Rubens, 1987). More importantly, in more than two-thirds of cases, metastases will not be limited to the skeleton, but rather subsequently occur to other organs and eventually cause death (Coleman, 2006; Coleman and Rubens, 1987; Coleman et al., 1998). This raises the possibility of secondary dissemination from the initial bone lesions to other sites. Indeed, recent genomic analyses concluded that the majority of metastases result from seeding from other metastases, rather than primary tumors (Brown et al., 2017; Gundem et al., 2015; Ullah et al., 2018). Thus, it is imperative to investigate further metastatic seeding from bone lesions, as it might lead to prevention of the terminal stage, multi-organ metastases that ultimately cause the vast majority of deaths.

Despite its potential clinical relevance, little is known about metastasis-to-metastasis seeding. Current preclinical models focus on seeding from primary tumors but cannot distinguish between additional sites of dissemination. We have recently developed an approach, termed intra-iliac artery injection (IIA), that selectively deliver cancer cells to hind limb bones via the external iliac artery (Wang et al., 2015, 2018; Yu et al., 2016). Although it skips the early steps of the metastasis cascade, it focuses on the initial seeding of tumor cells in the hind limbs, and allows the tracking of secondary metastases from bone to other organs. It is therefore a suitable model to investigate the clinical and biological roles played by bone lesions in multi-organ metastasis-to-metastasis seeding.

RESULTS

Temporally lagged multi-organ metastases in mice carrying IIA-introduced bone lesions of breast and prostate cancers

IIA injection has been employed to investigate early-stage bone colonization. Both aggressive (e.g., MDA-MB-231) and relatively indolent (e.g., MCF7) breast cancer cells can colonize bones albeit following different kinetics. In both cases, cancer cell distribution is highly bone-specific at early time points, allowing us to dissect cancer-bone interactions without the confounding effects of tumor burden in other organs (Figure 1A) (Wang et al., 2015, 2018). However, as bone lesions progress, metastases, as indicated by bioluminescence signals, begin to appear in other organs, including additional bones, lung, liver, kidney, and brain, usually 4–8 weeks after IIA injection of MDA-MB-231 cells (Figure 1B). Bioluminescence imaging provides sufficient sensitivity to detect metastases (Deroose et al., 2007). However, many factors such as lesion depth and optical properties of tissues may influence signal penetration. Thus, we used a number of other approaches to validate the presence of metastases in multiple types of tissues. These include positron emission tomography (PET) (Figure 1C), micro computed tomography (μCT) (Figures 1C and S1A), whole-tissue two-photon imaging (Figure S1B), immunofluorescence staining (Figure 1D and 1E), and histological staining (H&E) (Figure S1C). Compared to bioluminescence imaging, these approaches provided independent evidence, but are either less sensitive or non-quantitative (Deroose et al., 2007) (Figure S1A). Therefore, we also used quantitative PCR (qPCR) to detect human-specific DNA in dissected mouse tissues and confirmed that qPCR results and bioluminescence signal intensity values are highly correlative (Figures S1D and S1E). Of note, the spectrum of metastases covers multiple other bones (Figure 1D) and soft-tissue organs (Figure 1E). Taken together, our data support occurrence of multi-organ metastases in animals with IIA-introduced bone lesions.

This phenomenon is not specific for the highly invasive MDA-MB-231 cells, but was also observed in more indolent MCF7 cells and PC3 prostate cancer cells, as well as murine mammary carcinoma AT-3 cells in immunocompetent mice, albeit after a longer lag period for PC3 cells (8–12 weeks) (Figures 1F–1H and S1F).

As an independent approach to introduce bone lesions, we used intra-femoral (IF) injection that delivers cancer cells directly to bone marrow, bypassing the artery circulation involved in IIA injection. This approach also resulted in multi-organ metastases at late time points in both MDA-MB-231 and AT-3 models (Figures 1I and S1G). The frequency and distribution patterns of metastases were similar between intra-femoral and IIA injection models (Figures 1J and 1K). Thus, we hypothesize cancer cells in the bone microenvironment may gain capacity to further metastasize.

Figure 1. Multi-organ metastases in mice with bone lesions

(A) Diagram of intra-iliac artery (IIA) injection and representative bioluminescent images (BLI) showing the *in vivo* distribution of tumor cells after IIA injection of 1E5 MDA-MB-231 fLuc-mRFP cells.

(B and C) Representative *ex vivo* BLI images (B) and PET-μCT (C) on hindlimb and other tissues of the same animal with MDA-MB-231 cells inoculated in the right hindlimb after 8 weeks. R.H, right hindlimb; Lu, lung; L.H, left hindlimb; Li, liver; Ki, kidney; Sp, spleen; Br, brain; Ve, vertebrae; F.L, forelimbs; Ri, ribs; St, sternum; Cr, cranium.

(D and E) Representative immunofluorescent images of tumor lesions in various bones (D) and other organs (E). To obtain complete views of entire organs, smaller fields were acquired in tiles by mosaic scanning and then stitched by Zen. Scale bar, 20 μm.

(F–H) Representative BLI images of animals and tissues after IIA injection of 2E5 prostate cancer cells PC3 (F), 1E5 ER^+ breast cancer cells MCF7 (G), and 1E5 murine mammary carcinoma cells AT-3 (H) at the indicated time.

(I) Diagram of intra-femoral injection (IF) (left) and representative *ex vivo* BLI images of tissues from animals received 1E5 MDA-MB-231 cells (middle) or AT-3 cells (right) via IF injection.

(J and K) Heatmap of *ex vivo* BLI intensity and status of metastatic involvement on various types of tissues from animals carried MDA-MB-231 (J) and AT-3 (K) bone tumors. Columns, individual animal; rows, various tissues or status of multi-site metastases; Gray, no detectable lesion. n (# of mice): MDA-MB-231, 16 (IIA), 11 (IF); AT-3, 10 (IIA), 10 (IF). p values were assessed by Fisher's exact test on the ratio of metastasis while by Mann-Whitney test on the tumor burden.
See also Figure S1.

Bone lesions more readily give rise to multi-organ metastasis

The later-appearing multi-organ metastases may result from further dissemination of cancer cells in the initial bone lesions. Alternatively, they could also arise from cancer cells that leaked and escaped from bone capillaries during IIA or IF injection. In the latter case, the leaked cancer cells would enter the iliac vein and subsequently arrive in the lung capillaries. Indeed, there did appear to be bioluminescence signals in the lungs upon IIA injection (Figure 1A). To distinguish these probabilities, we performed intra-iliac vein (IIV) injection and compared the results to those of IIA injection at late time points. The IIV injection procedure should mimic the "leakage" from IIA injection, although this would allow many more cells to enter the venous system and be arrested in the lung capillaries (Figures 2A and S2A–S2C, compared to Figure 1A). As another relevant comparison, we also examined metastasis from orthotopic tumors transplanted into mammary fat pad (MFP) (Figures 2B, S2A, S2B, and S2D). Furthermore, in the case of ER^+ cells, recent studies suggest that intra-ductal injection provides a more "luminal" microenvironment and may promote spontaneous metastasis to other organs (Sflomos et al., 2016). As a result, specifically for MCF7 cells, the only ER^+ cancer model used in our study, we also included mouse intra-ductal (MIND) injection as an additional model. In all experiments, we used total bioluminescence signal intensity to evaluate tumor burdens at hind limbs (IIA and IF), lungs (IIV), and mammary fat pads (MFP and MIND), respectively. We attempted to assess multi-organ metastasis when the "primary lesions" reach a comparable level of bioluminescent intensity, simply to rule out the source tumor burden as a confounding factor in our comparisons. This was feasible for some models such as mammary tumors and bone lesions derived from MCF7 (Figure S2E). However, in other models, mammary tumors tend to grow much faster compared to lesions growing in other sites (Figures S2F and S2G). Therefore, we chose to end experiments at the same time point for all conditions. In all experiments, multi-organ metastases were examined well before animals became moribund. Taken together, we asked if secondary metastasis from bone lesions follows a faster kinetics and reaches a wider spectrum of target organs as compared to that from orthotopic tumors or lungs.

Strikingly, the answer to this question is evidently positive in all three tumor models examined (Figures 2C–2H). We assessed 11 organs including six other bones and five soft tissue organs for metastasis. Curiously, in many cases, counter-lateral hind limbs (designated as "L.Hindlimb" for "left hind limb" as the initial bone lesions were introduced to the right hind limb) are most frequently affected among all organs in IIA models. Lungs are also frequently affected in MDA-MB-231 and AT-3 models, by metastasis from both bone lesions and orthotopic tumors. However, it is striking to note that lung metastasis in IIA and IF models is comparable or even more severe as compared to that in IIV models, despite the fact that IIV injection delivers more cancer cells directly to lungs (Figure S2H). In fact, the normalized increase of tumor burden at lungs through IIA and IF are at least 10-fold more than that through IIV injection (e.g., Figure S2H), which strongly argue that bone microenvironment promotes secondary metastasis.

Cross-seeding of cancer cells from bone lesions to orthotopic tumors

Cancer cells may enter circulation and seed other tumor lesions or re-seed the original tumors (Kim et al., 2009). By using MDA-MB-231 cells tagged with different fluorescent proteins, we asked if bone lesions can cross-seed mammary tumors (Figure 3A). Interestingly, we observed that although orthotopic tumors can be readily seeded by cells derived from bone lesions, the reverse seeding rarely occurs (Figures 3B and 3C). This difference again highlights the enhanced metastatic aggressiveness of cancer cells in the bone microenvironment.

Parabiosis models support enhanced capacity of cancer cells to metastasize from bone to other organs

It is possible that IIA injection disturbs bone marrow and stimulates systemic effects that allow multi-organ metastases. For example, the injection might cause a transient efflux of bone marrow cells that can arrive at the distant organ to form pre-metastatic niche. To test this possibility, we used parabiosis to fuse the circulation between a bone lesion-carrying mouse (donor) and tumor-free mouse (recipient) 1 week after IIA injection. In parallel, we also performed parabiosis on donors that have received MFP injection and tumor-free recipients (Figure 3D). After 7 weeks, surgical separation was performed to allow time for metastasis development in the recipients. Subsequently, the organs of originally tumor-free recipients were collected and examined for metastases 4 months later. Only ~20% of recipients in the IIA group were found to harbor cancer cells in various organs (Figures 3E and 3F), mostly as microscopic disseminated tumor cells (Figure 3G), indicating that the fusion of circulation system is not efficient for metastatic seeds to cross over from donor to recipient. However, in the MFP comparison group, no metastatic cells were detected (Figures 3F, S3A, and S3B), and the difference is statistically significant. Therefore, the parabiosis data also support the hypothesis that the bone microenvironment invigorates further metastasis, and this effect is unlikely to be due to IIA injection-related systemic influence.

An evolving barcode system revealed the phylogenetic relationships between initial bone lesions and secondary metastases

Barcoding has become widely used to elucidate clonal evolution in tumor progression and therapies. An evolving barcoding system has recently been invented for multiple parallel lineage tracing (Kalhor et al., 2017, 2018). It is based on CRISPR/Cas9 system but utilizes guide RNAs that are adjacent to specific protospacer adjacent motif (PAM) in their genomic locus, thereby allowing Cas9 to mutate its own guide RNAs. These variant guide RNAs are named homing guide RNAs (hgRNAs). When Cas9 is inducibly expressed, hgRNA sequences will randomly drift, serving as evolving barcodes (Figure 4A). A preliminary *in vitro* experiment demonstrated that the diversity of barcodes (measured as Shannon entropy) is a function of duration of Cas9 expression (Figures 4B and S4A).

We introduced this system into MDA-MB-231 and AT-3 cells, and transplanted them into mammary fat pads of nude and wild-type C57BL/6 mice, respectively. When orthotopic tumors

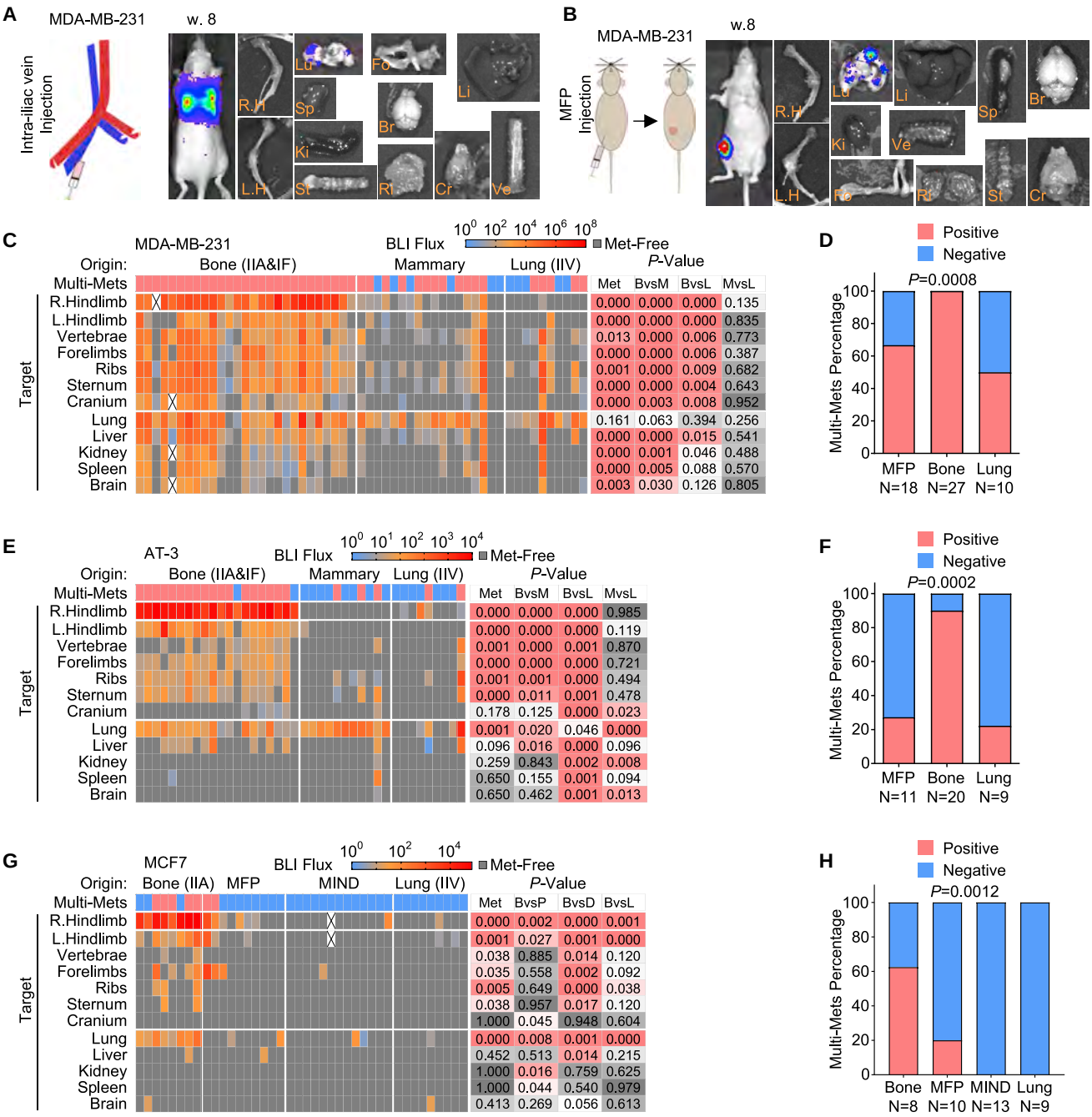

Figure 2. Bone microenvironment promotes further metastasis

(A) Diagram of intra-iliac vein (IIV) injection and representative BLI images of animals and tissues 8 weeks after IIV injection of 1E5 MDA-MB-231 cells.

(B) Diagram of mammary fat pad (MFP) implantation and representative BLI images of animals and tissues 8 weeks after MFP implantation of 1E5 MDA-MB-231 cells.

(C and D) Comparison of metastatic pattern and tumor burden (C) and the ratio of multi-site metastasis (D) in animals with bone (IIA/IF), lung (IIV) or mammary (MFP) tumors of MDA-MB-231 cells. n (# of mice) = 27 (bone); 18 (MFP); 10 (lung).

(E and F) Comparison of metastatic pattern and tumor burden (E) and the ratio of multi-site metastasis (F) in animals with bone (IIA/IF), lung (IIV) or mammary (MFP) tumors of AT-3 cells. n (# of mice) = 20 (bone); 11 (MFP); 9 (lung).

(G and H) Comparison of metastatic pattern and tumor burden (G) and the ratio of multi-site metastasis (H) in animals with bone (IIA), lung (IIV) or mammary (MFP or MIND) tumors of MCF7 cells. n (# of mice) = 8 (bone); 10 (MFP); 13 (MIND); 9 (lung).

p values were assessed by χ^2 test in (C)–(H) on the ratio of metastasis; by uncorrected Dunn's test following Kruskal-Wallis test in (C), (E), and (H) on the tumor burden.

See also Figure S2.

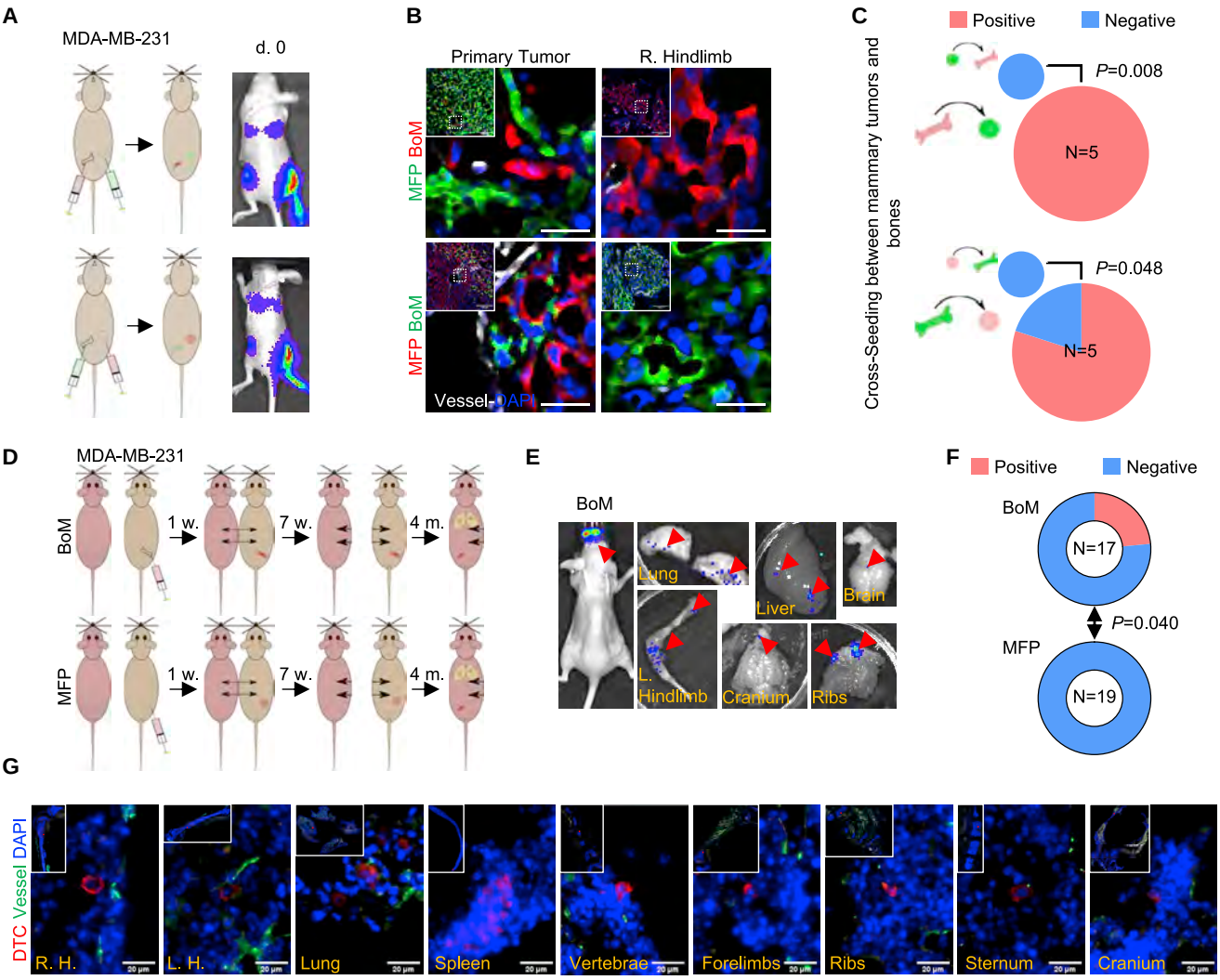

Figure 3. Cross-seeding and parabiosis experiments support the promoting effects of bone microenvironment on further dissemination

(A) Experimental design of cross-seeding experiment between mammary and bone tumors of mRFP or EGFP tagged MDA-MB-231 cells. Upper: mRFP (IIA), EGFP (MFP). Lower: EGFP (IIA), mRFP (MFP).

(B) Representative confocal images showing the cross-seeding between bone and mammary tumors. Scale bar, 20 μm. n (# of mice) = 5 for each arm.

(C) Incidence of cross-seeding between bone and mammary tumors.

(D) Experimental design of parabiosis models to compare the metastatic capacity of bone and mammary tumors. n (# of mice) = 17 (BoM); 19 (MFP).

(E) Representative BLI images of metastatic lesions in recipient mice parabiotic with mice bearing bone metastases.

(F) Ratio of recipients with metastasis in bone and mammary tumor groups, as determined by BLI imaging.

(G) Representative immunofluorescent images on tissues from recipients of bone tumor group. To obtain complete views of entire organs, smaller fields were acquired in tiles by mosaic scanning and then stitched by Zen. Scale bar, 20 μm. Tissues from 6 animals were examined.

p values were assessed by Fisher's exact test in (C) and (F).

See also Figure S3.

reach 1 cm^3, we resected the tumors and induced Cas9 by doxycycline. It should be noted that the orthotopic tumors already harbored a high diversity of mutant barcodes presumably due to leakage of Cas9 expression. This served as an initial barcode repertoire that enabled us to distinguish distinct clones that metastasize from orthotopic tumors to various organs. Further Cas9 expression yielded new mutations for delineation of parent-child relationship among lesions (Figure 4C). We rationalize that the diversity of barcodes, or the Shannon entropy, in a metastasis should reflect the "age" of metastasis. When secondary metastasis occurs, child metastases will inherit only a subset of barcodes causing a reduction of Shannon entropy. Therefore, among genetically related metastases indicated by sharing common mutant barcodes, those with higher Shannon entropy are more likely to be parental (Figure 4C). This can be supported by the observation that primary bone lesions possess higher entropy than those secondary metastases in IIA model (Figure S4B).

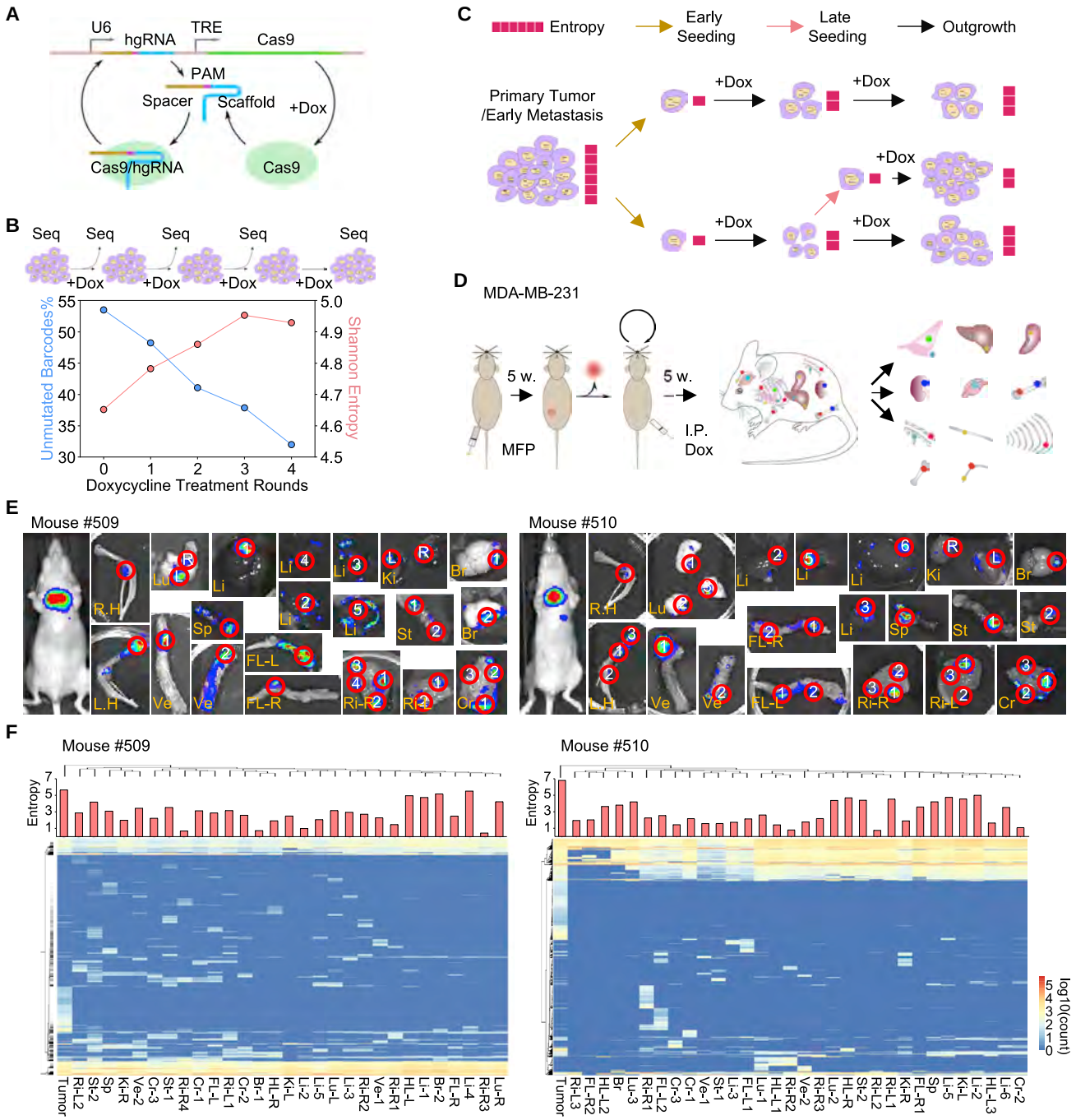

Figure 4. *In vivo* barcoding of spontaneous metastases with hgRNAs

(A) Principle of the evolving barcode system comprised of hgRNAs and inducible Crispr-Cas9.

(B) Ratio of unmutated barcode and Shannon entropy in MDA-MB-231 cells upon multiple rounds of doxycycline treatment *in vitro*.

(C) Schematics showing the rationale of using evolving barcodes to infer the evolution of metastatic lesions and the timing of seeding events. Barcode diversity decreases during the seeding process. Children metastases inherit a subset of signature barcodes from parental tumors. Upon Cas9 activation, barcodes start evolving and regain diversity. Diversity of barcodes can therefore infer the relative timing of seeding, and phylogenetically related metastases share a subset of signature barcodes.

(D and E) Design of *in vivo* barcoding experiment (D) and representative BLI images (E) of metastatic lesions from MDA-MB-231 tumors.

(F) Feature matrix of mutation events in MDA-MB-231 metastatic samples.

See also Figure S4 and Table S1.

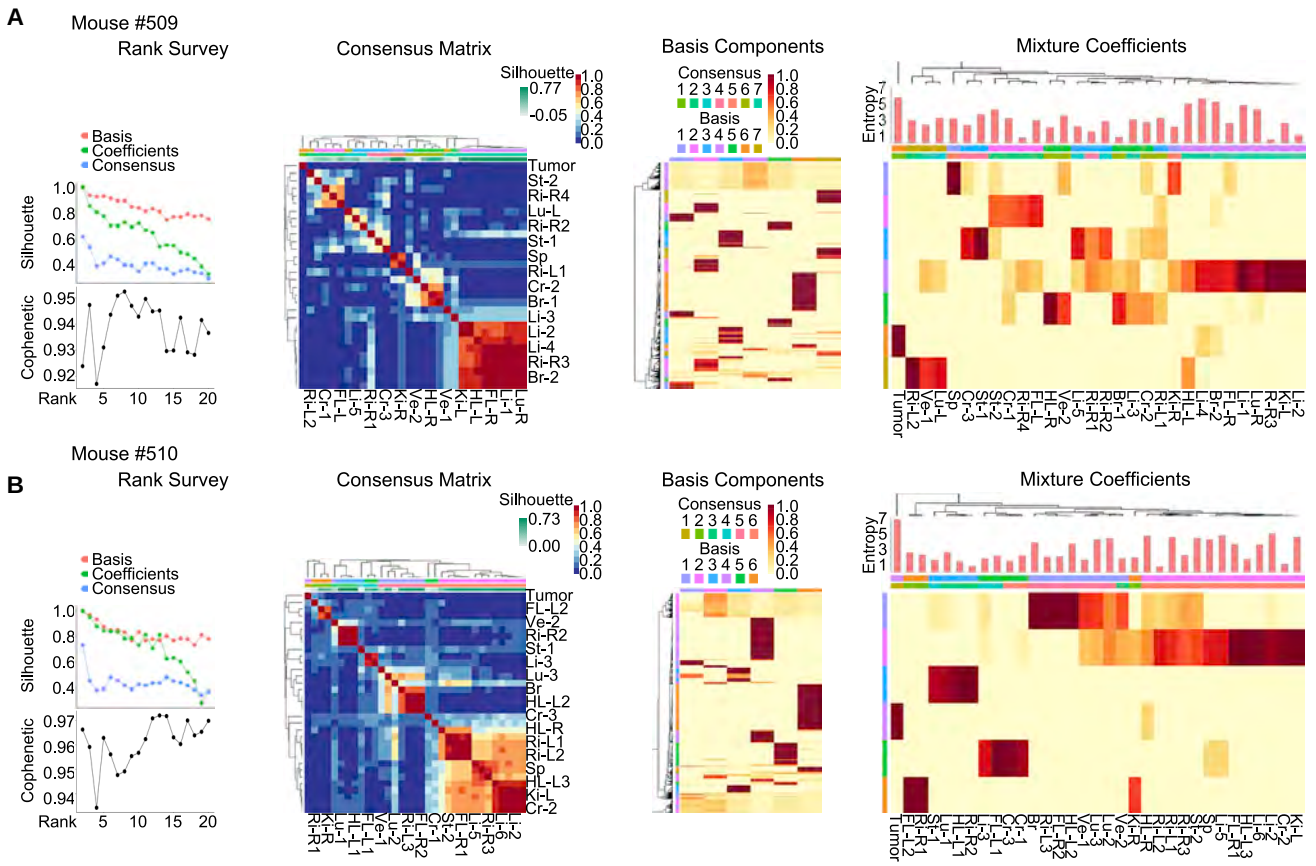

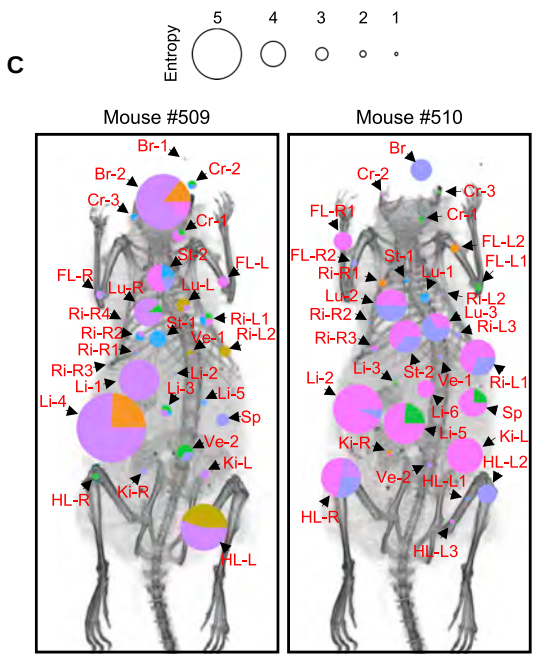

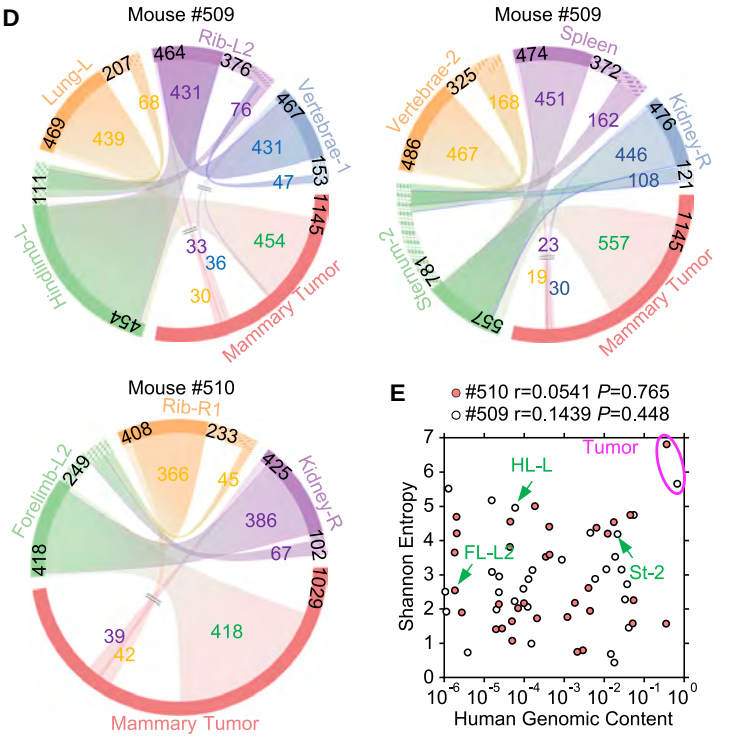

(legend on next page)

We isolated 29, 32, 9, and 17 metastases from two mice bearing MDA-MB-231 and two mice bearing AT3 tumors, respectively (Figures 4D, 4E, and S4C; Table S1). Sequencing of the barcodes carried by these metastases in combination of the analysis of the timing of seeding as indicated by the Shannon entropy of barcodes led to profound findings. First, in line with a previous study (Echeverria et al., 2018), multi-organ metastases are not genetically grouped according to sites of metastases at the terminal stage (Figures 4F and S4D). Nonnegative matrix factorization (NMF) analysis of mutant barcodes suggested the early disseminated metastases, which have the highest level of Shannon entropy, were featured with a common cluster of mutant barcodes irrespective of their locations, especially in AT-3 models (Figures 5A–5C and S5A–S5C). This is evidence against organotropism in the late stage of metastatic progression in mouse models. Second, most metastases are potentially multiclonal as indicated by multiple clusters of independent mutant barcodes (Figures 5C and S5C). Third, putative parent-child relationship between metastases with unique mutant barcodes clearly exemplified secondary metastatic seeding from bone to other distant sites (Figures 5D and S5D) in both models. Finally, we did not observe a clear correlation between tumor burden and Shannon entropy across different metastases, and the putative funder metastases can be small in tumor burden while diversified in barcode composition, suggesting that asymptomatic metastases might also seed further metastases (Figures 5E and S5E). Taken together, these data reveal potential widespread metastasis-to-metastasis seeding and support that secondary metastases from the bone to other distant organs happen in a natural metastatic cascade.

The bone microenvironment promotes further metastasis by enhancing cancer cell stemness and plasticity

Organotropism is an important feature of metastasis. Clonal selection appears to play an important role in organ-specific metastasis, which has been intensively studied (Bos et al., 2009; Kang et al., 2003; Minn et al., 2005; Vanharanta and Massagué, 2013). Here, the metastasis-promoting effects of the bone microenvironment appear to be multi-organ and do not show specific organ-tropism. In an accompanied study, we discovered profound phenotypic shift of ER^+ breast cancer cells in the bone microenvironment, which included loss of luminal features and gain of stem cell-like properties (Bado et al., 2021). This shift is expected to promote further metastases (Gupta et al., 2019; Ye and Weinberg, 2015). Therefore, we hypothesize that the enhancement of metastasis may be partly through an epigenomic dedifferentiation process.

To test this possibility, we compared the metastasis capacity of a genetically identical SCP of MDA-MB-231 cells and its derivatives entrained by different microenvironments (Figures S6A and S6B). Based on a previous study (Minn et al., 2005), we picked a non-metastatic SCP termed SCP21. SCP21 cells were introduced to mammary fat pads, lungs, and hind limb bones to establish tumors. After 6 weeks, entrained cancer cells were extracted from these organs for further experiments (Figure 6A). We used intra-cardiac injection to simultaneously deliver cancer cells to multiple organs (Figure 6A). Compared to the mammary fat pad- and lung-entrained counterparts, bone-entrained SCP21 was more capable of colonizing distant organs and gave rise to much higher tumor burden in multiple sites as determined by bioluminescence (Figures 6A–6C). In mice subjected to dissection and *ex vivo* bioluminescent imaging, significantly more and bigger lesions were observed from mice received bone-entrained SCP21 cells in both skeletal and visceral tissues (Figures S6C–S6E), suggesting an increase of overall metastatic capacity rather than bone tropism in tumor cells exposed to bone environment.

Inspired by the accompanied study (Bado et al., 2021), we examined stemness markers (Al-Hajj et al., 2003; Charafe-Jauffret et al., 2009) of SCP21 cells entrained in different microenvironments. Interestingly, bone-entrained cells appeared to express a higher level of both ALDH1 activity and CD44 expression (Figures 6D and 6E). In addition, bone-entrained SCP21 cells increased expression of multiple proteins involved in epithelial-mesenchymal transition (EMT) and in pathways shown to mediate the effects of bone microenvironment on ER^+ cancer cells in our accompanied study, including FGFR1, PDGFRβ, EZH2, SLUG, and ZEB1 (Figures 6F and S6F). These data suggest that similar mechanisms may be at work to induce cancer cell stemness and plasticity in this ER^- model.

Indeed, when the same approaches were applied to the SCP2 derivatives of MCF7 cells. Bone entrained MCF7-SCP2 cells showed increased initial survival and faster metastatic growth after intra-cardiac injection (Figures 6G–6I) and increased level of ALDH1 activity and CD44 expression (Figures 6J and 6K). In this epithelial model, we also observed a hybrid EMT phenotype (Figure S6G), as also elaborated in our associated study (Bado et al., 2021). It should be noted that, in this series of experiments, lung-derived subline was not developed due to the lack of lung colonization for MCF7-SCP2 cells.

In addition to cancer cells that are manually extracted from various organs, we examined naturally occurred circulating tumor cells (CTCs) emitted from bone lesions versus mammary tumors. Not surprisingly, bone lesions generated a higher number of CTCs, probably due to the more permeable vascular structures or survival advantage conferred by the bone.

Figure 5. NMF analysis of evolving barcodes delineates metastatic spread

(A and B) Plots of NMF rank survey, consensus matrix, basis components matrix and mixture coefficients matrix of 200 NMF runs on the barcodes from MDA-MB-231 metastatic lesions.

(C) Body map depicting the basis composition of MDA-MB-231 metastatic lesions.

(D) Chord diagrams illustrating the composition flow of barcode mutations between primary tumors and selected MDA-MB-231 metastatic lesions.

(E) Correlation plot of Shannon entropy and tumor burden on MDA-MB-231 samples. The tumor burden was indicated by human genomic content determined by q-PCR. Spearman r and p values were indicated.

See also Figure S5.

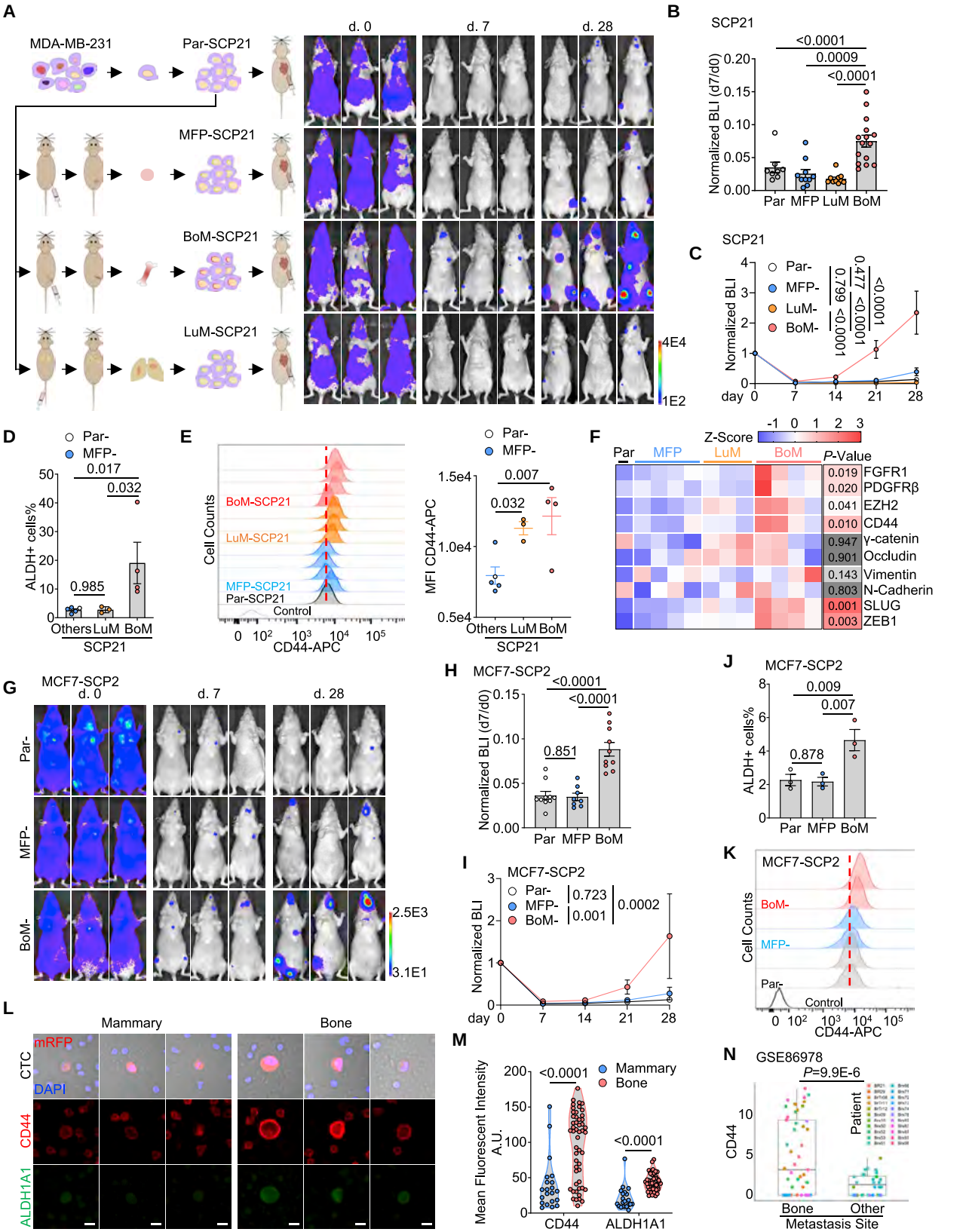

(legend on next page)

However, on top of the higher number, CTCs from bone lesions also express higher quantity of CD44 and ALDH1 (Figures 6L and 6M), suggesting increased stemness.

Finally, we also interrogated CD44 expression in a single-cell RNA sequencing (RNA-seq) dataset of CTCs derived from breast cancer patients. When patients were divided into two groups—those carrying bone metastasis versus those carrying other metastases, significantly higher expression of CD44 was observed in the former (Figure 6N) (Aceto et al., 2018), providing clinical support for our hypothesis that the bone microenvironment promotes tumor cell stemness and plasticity, and thereby invigorate further metastasis.

EZH2 in cancer cells orchestrates the effect of bone microenvironment in secondary metastasis

Because EZH2 was revealed to play a central role in loss of ER and gain of plasticity in ER$^+$ models in the accompanied study (Bado et al., 2021), we asked if it also mediates secondary metastasis. The frequency of ALDH1$^+$ cells and the expression of mesenchymal and stemness markers in bone-entrained SCP21 cells were also significantly decreased upon treatment of an EZH2 inhibitor (EPZ) used in our accompanied study (Figures S7A–S7C), supporting EZH2 as an upstream regulator the observed phenotypic shift.

In addition to expression, we used an EZH2 target gene signature (Lu et al., 2010) to deduce EZH2 activities. This signature was then applied to RNA-seq transcriptomic profiling of SCP21 cells subjected to various treatments or entrained in different organs. EPZ treatment relieved the suppression of signature genes, resulting in higher expression (Figure S7D), which supported the validity of the signature. We then compared cells entrained in bone lesions versus mammary gland tumors or lung metastasis and observed significantly higher EZH2 activity in the bone-entrained cells (Figure 7A). Importantly, bone-induced changes to both EZH2 activity and frequency of ALDH1$^+$ cells appeared to be reversible, as *in vitro* passages led to progressive loss of these traits (Figures 7B and 7C). Other bone microenvironment-induced factors upstream of EZH2 (e.g., FGFR1 and PDGFRβ) (Kottakis et al., 2011; Yue et al., 2019) also exhibited transient increased expression in bone-entrained cells (Figures 7D and S7E). Taken together, these data further suggest the potential role of EZH2 in secondary metastasis from bone lesions.

Remarkably, transient treatment of EPZ before intra-cardiac injection, which did not suppress the growth of tumor cells *in vitro* (Figure S7F), completely abolished the enhanced metastasis of bone-entrained SCP21 cells (Figures 7E–7G) and MCF7-SCP2 cells (Figures 7H–7K) *in vivo*, again demonstrating that the observed effects of bone microenvironment is not through clonal selection, but rather epigenomic reprogramming driven by EZH2.

Finally, to confirm the cancer cell-intrinsic role of EZH2 during this process, we generated inducible knockdown of EZH2 (Figure S7G), that also slightly affected downstream expression of plasticity factors and stem cell markers (Figures S7G and S7H), but did not alter cancer cell growth rate *in vitro* (Figure S7I). Induction of knockdown was initiated after bone lesions were introduced for one week (Figures 7L, and S7J). Interestingly, whereas EZH2 knockdown did not alter primary bone lesion development (Figure 7M), it dramatically reduced secondary metastasis to other organs (Figure 7N). Taken together, these aforementioned results strongly implicate EZH2 as a master regulator of secondary metastases from bone lesions.

DISCUSSION

In this study, based on the IIA injection technique and through multiple independent approaches, we demonstrated that the bone microenvironment not only permits cancer cells to further disseminate but also appears to augment this process. A key question that remains is the timing of secondary metastasis spread out of the initial bone lesions: whether this occurs before or after the bone lesions become symptomatic and clinically detectable. The answer will determine if therapeutic interventions should be implemented in adjuvant or metastatic settings, respectively. Moreover, if further seeding occurs before bone lesions become overt, it raises the possibility that metastases in other organs might arise from asymptomatic bone metastases, which might warrant further investigations. Indeed, it has been reported that DTCs in bone marrow of early breast cancer patients enrich stem cell-like population (Alix-Panabieres et al.,

Figure 6. Bone-entraining boosts the metastatic capacity of single cell-derived cancer cells

(A) Experimental design (left) and representative BLI images (right) to test the metastatic capacity of mammary, lung, or bone-entrained SCP21s.

(B) Normalized whole-body BLI intensity 7 days after intra-cardiac (IC) injection of same number of MFP-, LuM-, BoM-, or Par-SCP21 cells.

(C) Colonization kinetics of MFP-, LuM-, BoM-, and Par-SCP21 cells after IC injection. n (# of mice) = 8 (Par); 10 (MFP); 15 (BoM); 10 (LuM).

(D) Percentage of ALDH$^+$ population in MFP-, LuM-, BoM-, and Par-SCP21 cells by flow cytometry.

(E) Histogram (left) and median fluorescent intensity (MFI) (right) of surface CD44 protein in MFP-, LuM-, BoM- and Par-SCP21 cells by flow cytometry.

(F) Expression levels of proteins in Par- and organ-entrained SCP21s. Protein levels were quantified and converted into *Z* score from three or four western blottings.

(G–I) Representative BLI images (G), normalized BLI intensity at day 7 (H), and the colonization kinetics (I) of MFP-, BoM-, and Par- MCF7-SCP2 cells after I.C. injection. n (# of mice) = 10 (Par); 8 (MFP); 10 (BoM).

(J and K) Percentage of ALDH$^+$ population (J) and expression of surface CD44 (K) in MFP-, BoM-, and Par- MCF7-SCP2 cells by flow cytometry. n (# of repeats) = 3 (J); 2 (K).

(L and M) Representative fluorescent images (L) and quantification (M) of CD44 and ALDH1A1 expression on CTCs from NRG mice bearing MDA-MB-231 cells derived mammary or bone tumors. CTCs were pooled from 5 blood samples. Scale bar, 10 μm.

(N) Expression levels of CD44 mRNA in CTCs from breast cancer patients with bone metastases or other metastases (GSE86978).

Data are represented as mean ± SEM in (B), (C), (D), (E), (H), (I) and (J). p values were assessed by Fisher's LSD test following one-way ANOVA test in (B), (D), (E), (H), and (J); by Fisher's LSD test post two-way ANOVA test in (C) and (I); by Student's t test in (F); by Mann-Whitney test in (M) and (N).

See also Figure S6.

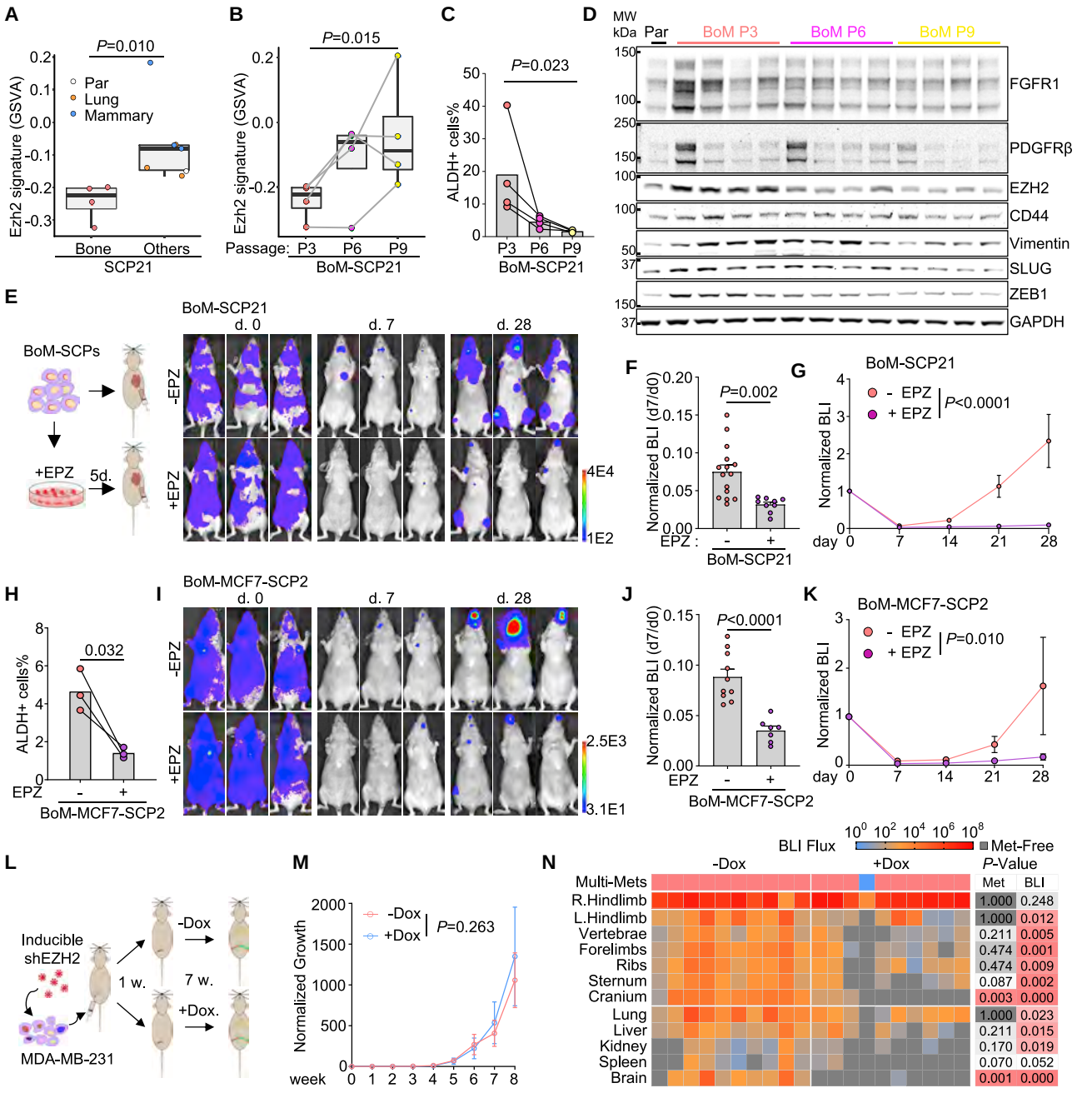

Figure 7. Secondary metastasis from bone lesions is dependent on EZH2 mediated epigenomic reprograming

(A) Levels of EZH2 signature genes (GSVA) in bone entrained and other SCP21 cells.

(B) Levels of EZH2 signature genes in bone entrained-SCP21 cells after different passages *in vitro*.

(C) Percentage of ALDH1$^+$ population in bone entrained-SCP21 cells at different passages.

(D) Representative western blotting of proteins in bone entrained-SCP21 cells after different passages.

(E–G) The schematic diagram and representative BLI images (E), normalized BLI intensity at day 7 (F), and the colonization kinetics (G) of BoM-SCP21 cells with *in vitro* EPZ011989 (EPZ) treatment before IC injection. Non-treated BoM-SCP21 cells were used as control. n (# of mice) = 15 (−EPZ); 9 (+EPZ).

(H) Comparison of ALDH1+ cells in EPZ treated and non-treated BoM-MCF7-SCP2 cells by flow cytometry. n (# of replicate) = 3.

(I–K) Representative BLI images (I), normalized BLI intensity at day 7 (J), and the colonization kinetics (K) of BoM-MCF7-SCP2 cells with *in vitro* treatment of EPZ before IC injection. Non-treated BoM-MCF7-SCP2 cells were used as control. n (# of mice) = 10 (−EPZ); 7 (+EPZ).

(L) Experimental design assessing the multi-site metastases from bone lesions with inducible depletion of EZH2.

(M) Growth kinetics of the primary bone lesions in mice receiving doxycycline or control water, assessed by *in vivo* BLI imaging. BLI intensities at right hindlimbs were normalized to the mean intensity at day 0. n (# of mice) = 10 for each arm.

(legend continued on next page)

2007; Balic et al., 2006), supporting that asymptomatic bone micrometastases are potentially capable of metastasizing before being diagnosed. In this study, our evolving barcode strategy exemplified potential metastases from bone to other organs. Interestingly, we found that the putative parental metastases could remain small (Figures 5E and S5E), which may suggest that further dissemination might occur before diagnosis of existing lesions. Future studies will be needed to precisely determine the onset of secondary metastasis from bones.

The fact that the genetically homogeneous SCP cells became more metastatic after lodging into the bone microenvironment suggests a mechanism distinct from genetic selection. Remarkably, this phenotype persists even after *in vitro* expansion, so it is relatively stable and suggests an epigenomic reprogramming process. We propose that this epigenetic mechanism may act in concert with the genetic selection process. Specifically, the organ-specific metastatic traits may pre-exist in cancer cell populations (Minn et al., 2005; Zhang et al., 2013) and determine the first site of metastatic seeding. The epigenomic alterations will then occur once interactions with specific microenvironment niches are established and when cancer cells become exposed chronically to the foreign milieu of distant organs. Our data suggest that such alterations drive a second wave of metastases in a less organ-specific manner. This may explain why terminal stage of breast cancer is often associated with multiple metastases (Disibio and French, 2008).

Here, we suggested that the enhanced EZH2 activity underpins the epigenetic reprograming of tumor cells in bone microenvironment for further metastases. EZH2 maintains the de-differentiated and stem cell-like status of breast cancer cells by repressing the lineage-specific transcriptional programs (Chang et al., 2011; Gonzalez et al., 2014). Pharmacologically or genetically targeting EZH2 has been reported to inhibit tumor growth, therapeutic resistance, and metastases with different efficacies in preclinical models (Hirukawa et al., 2018; Ku et al., 2017; Ma et al., 2020; Zhang et al., 2020). It was noted that in our models, EZH2 inhibition could not suppress the cell growth *in vitro* or in the primary injection site, whereas both the transient treatment of EZH2 inhibitor or inducible knockdown of EZH2 in cancer cells dramatically decreased secondary metastasis, suggesting targeting EZH2 may block the metastatic spread rather than the tumor growth.

In the clinic, some bone metastases can be managed for years without further progression, while others quickly develop therapeutic resistance and are associated with subsequent metastases in other organs (Coleman, 2006). These different behaviors may suggest different subtypes of cancers that are yet to be characterized and distinguished. Alternatively, there may be a transition between these phenotypes. In fact, depending on different interaction partners, the same cancer cells may exist in different status in the bone. For instance, although endothelial cells may keep cancer cells in dormancy (Ghajar et al., 2013; Price et al., 2016), osteogenic cells promote their proliferation and progression toward micrometastases (Wang et al., 2015, 2018). Therefore, it is possible that the transition from indolent to aggressive behaviors is underpinned by an alteration of specific microenvironment niches. Detailed analyses of such alteration will lead to unprecedented insights into the metastatic progression.

Limitations the study

In this study, we did not provide direct clinical evidence that bone metastasis can seed other metastases in cancer patients. Although this is reported in several previous studies (Brown et al., 2017; Gundem et al., 2015; Ullah et al., 2018), the prevalence of secondary metastases seeded from bone lesions remains to be determined in patients. Future genomic studies with improved depth and informatics will likely dissect this process in greater depth and elucidate spatiotemporal paths of metastasis. The evolving barcode strategy was useful in tracing metastatic evolution. The most striking and robust finding from these experiments is that genetically closely related metastases do not localize in the same type of tissues and are usually highly distinct from orthotopic tumors. This in principle argues against independent seeding events from primary tumors and supports metastasis-to-metastasis seeding. However, the deduction of specific parental-child relationship based on Shannon entropy is intuitive and qualitative, and needs to be analyzed by more quantitative models in future work.

We principally demonstrated that compared to lungs, bones are more capable of promoting secondary metastasis. However, further studies will be required to determine whether other organs, such as liver and lymph nodes, might also exert similar effects on metastatic spread. We postulate that two factors may regulate an organ's capacity to promote secondary metastases. First, the initial wave of organotropic metastasis will pose a selection of metastatic seeds that arrive and survive in a specific organ. Second, the subsequent interactions with resident cells will induce adaptive epigenetic changes on top of the genetic selection, which together dictate whether the metastatic journey may extend to other organs.

Although data presented in this study indicate that cancer cells colonizing the bone acquire intrinsic traits for further dissemination, we cannot rule out systemic effects that may also contribute to this process. At the late stage, bone metastases are known to cause strong systemic abnormality such as cachexia (Waning et al., 2015), which may influence secondary metastasis. Even at early stages before bone metastases stimulate severe symptoms, the disturbance of micrometastases to hematopoietic cell niches may mobilize certain blood cells to migrate to distant organs, which may in turn result in altered metastatic behaviors (Peinado et al., 2017). These possibilities will need to be tested in future research.

(N) Heatmap of *ex vivo* BLI intensity and status of metastatic involvement in tissues from animals with EZH2 depleted or control bone metastases.
Data are represented as mean ± SEM in (F), (G), (J), (K), and (M). p values were assessed by Student's t test in (A), (F), and (J); by test for linear trend following repeat measure one-way ANOVA in (B) and (C); by LSD test following two-way ANOVA in (G), (K), and (M); by ratio paired t test in (H); by Fisher's exact test on the ratio of metastatic involvement and Mann-Whitney test on BLI intensity in (N).
See also Figure S7.

STAR★METHODS

Detailed methods are provided in the online version of this paper and include the following:

- KEY RESOURCES TABLE
- RESOURCE AVAILABILITY
  - Lead contact
  - Materials availability
  - Data and code availability
- EXPERIMENTAL MODEL AND SUBJECT DETAILS
  - Cell lines and Cell Culture
  - Animals
- METHOD DETAILS
  - Plasmid Construction
  - Lentiviral Production and Transduction
  - *In vitro* activation of hgRNA barcodes
  - Intra-iliac artery and Intra-iliac vein Injection
  - Intra-femoral and Intra-Cardiac Injection
  - Mammary Fat Pad and Intra-Ductal Injection
  - Parabiosis and Reverse Procedure
  - *In vivo* activation of hgRNA barcodes
  - Bioluminescence Imaging and Tissue Collection
  - Small Animal PET-CT Scanning
  - Deep Imaging of Intact Tissues
  - Immunofluorescent Staining
  - Genomic DNA Extraction from Tissues and Cells
  - Amplification and Sequencing of hgRNA Barcodes
  - Evolving Barcode Data Processing
  - Non-negative matrix factorization analysis
  - Assessment of Metastasis of Organ-entrained SCPs
  - Flow Cytometry
  - RNA and Protein Extraction and Quantification
  - RNA-Sequencing and Whole Exome Sequencing
  - Capture and Staining of CTCs
- QUANTIFICATION AND STATISTICAL ANALYSIS

SUPPLEMENTAL INFORMATION

Supplemental information can be found online at https://doi.org/10.1016/j.cell.2021.03.011.

ACKNOWLEDGMENTS

We would like to thank Zhang Laboratory members Dr. Lin Tian and Dr. Reza Kalhor for insightful discussion. Thanks also go to Epizyme (Cambridge, MA) for providing the EZH2 inhibitor EPZ-011989. We also acknowledge the Pathology Core of Lester and Sue Smith Breast Center, the Optical Imaging & Vital Microscopy (OiVM) core, the Genomic and RNA profiling core at Baylor College of Medicine, and Small Animal Imaging Facility (SAIF) core at Texas Children Hospital. X.H.-F.Z. is supported by US Department of Defense (DAMD W81XWH-16-1-0073 and DAMD W81XWH-20-1-0375), NCI (CA183878, CA227904, CA221946, and CA251950), the Breast Cancer Research Foundation, and McNair Foundation. S.S. is a recipient of CPRIT Training Grant (RP160283). S.T.C.W. and Jiasong Li are supported in part by NCI (U01CA252553), the John S. Dunn Research Foundation, and T.T. and W.F. Chao Center for BRAIN. C.C. is supported by the CPRIT Scholar Award (RR160009). This project was supported by the RNA In Situ Hybridization Core with a Shared Instrumentation grant from the NIH (1S10OD016167), the Cytometry and Cell Sorting Core with funding from the CPRIT Core Facility Support Award (CPRIT-RP180672), and the expert assistance of Dr. Cecilia Ljungberg and Joel M. Sederstrom at Baylor College of Medicine.

AUTHOR CONTRIBUTIONS

Conceptualization and Methodology, W.Z., I.L.B., J.H., H.W., Z.L., and X.H.-F.Z.; Investigation, Formal Analysis and Validation, W.Z., I.L.B., J.H., Y.-W.W., L.W., H.W., Y.G., Z.X., X.H., B.M.L., R.A.-O., L.L., Jiasong Li, L.Y., H.C.L., M.N., Jun Liu, W.J., Z.L., and X.H.-F.Z.; Resources, Y.L., S.T.C.W., C.C., Z.L., and X.H.-F.Z.; Software, Data Curation, and Visualization, W.Z., I.L.B., J.H., Y.-W.W., H.-H.J., R.A.-O., L.L, S.S., Z.L., and X.H.-F.Z.; Writing – Original Draft, W.Z., I.L.B., J.H., and X.H.-F.Z.; Writing – Review & Editing, W.Z., H.C.L., S.T.C.W., and X.H.-F.Z.; Supervision, X.H.-F.Z.; Project Administration, W.Z. and X.H.-F.Z.; Funding Acquisition, S.T.C.W., C.C., and X.H.-F.Z.

DECLARATION OF INTERESTS

The authors declare no competing interests.

Received: September 12, 2019
Revised: November 30, 2020
Accepted: March 4, 2021
Published: April 19, 2021

REFERENCES

Aceto, N., Bardia, A., Wittner, B.S., Donaldson, M.C., O'Keefe, R., Engstrom, A., Bersani, F., Zheng, Y., Comaills, V., Niederhoffer, K., et al. (2018). AR expression in breast cancer CTCs associates with bone metastases. Mol. Cancer Res. *16*, 720–727.

Afgan, E., Baker, D., Batut, B., van den Beek, M., Bouvier, D., Cech, M., Chilton, J., Clements, D., Coraor, N., Grüning, B.A., et al. (2018). The Galaxy platform for accessible, reproducible and collaborative biomedical analyses: 2018 update. Nucleic Acids Res. *46* (W1), W537–W544.

Al-Hajj, M., Wicha, M.S., Benito-Hernandez, A., Morrison, S.J., and Clarke, M.F. (2003). Prospective identification of tumorigenic breast cancer cells. Proc. Natl. Acad. Sci. USA *100*, 3983–3988.

Alix-Panabières, C., Vendrell, J.-P., Pellé, O., Rebillard, X., Riethdorf, S., Müller, V., Fabbro, M., and Pantel, K. (2007). Detection and characterization of putative metastatic precursor cells in cancer patients. Clin. Chem. *53*, 537–539.

Andor, N., Harness, J.V., Müller, S., Mewes, H.W., and Petritsch, C. (2014). EXPANDS: expanding ploidy and allele frequency on nested subpopulations. Bioinformatics *30*, 50–60.

Bado, I.L., Zhang, W., Hu, J., Xu, Z., Wang, H., Sarkar, P., Li, L., Wan, Y.-W., Liu, J., Wu, W., et al. (2021). Impact of the bone microenvironment on phenotypic plasticity of ER+ breast cancer cells. Dev. Cell *56*, 1100–1117.

Balic, M., Lin, H., Young, L., Hawes, D., Giuliano, A., McNamara, G., Datar, R.H., and Cote, R.J. (2006). Most early disseminated cancer cells detected in bone marrow of breast cancer patients have a putative breast cancer stem cell phenotype. Clin. Cancer Res. *12*, 5615–5621.

Barger, C.J., Branick, C., Chee, L., and Karpf, A.R. (2019). Pan-Cancer Analyses Reveal Genomic Features of FOXM1 Overexpression in Cancer. Cancers (Basel) *11*, 251.

Bos, P.D., Zhang, X.H.F., Nadal, C., Shu, W., Gomis, R.R., Nguyen, D.X., Minn, A.J., van de Vijver, M.J., Gerald, W.L., Foekens, J.A., and Massagué, J. (2009). Genes that mediate breast cancer metastasis to the brain. Nature *459*, 1005–1009.

Boyce, B.F., Yoneda, T., and Guise, T.A. (1999). Factors regulating the growth of metastatic cancer in bone. Endocr. Relat. Cancer *6*, 333–347.

Brown, D., Smeets, D., Székely, B., Larsimont, D., Marcell Szász, A., Adnet, P.Y., Rothé, F., Rouas, G., Nagy, Z.I., Faragó, Z., et al. (2017). Phylogenetic analysis of metastatic progression in breast cancer using somatic mutations and copy number aberrations. Nat. Commun. *8*, 25–29.

Chang, C.J., Yang, J.Y., Xia, W., Chen, C.T., Xie, X., Chao, C.H., Woodward, W.A., Hsu, J.M., Hortobagyi, G.N., and Hung, M.C. (2011). EZH2 promotes expansion of breast tumor initiating cells through activation of RAF1-β-catenin signaling. Cancer Cell *19*, 86–100.

Charafe-Jauffret, E., Ginestier, C., Iovino, F., Wicinski, J., Cervera, N., Finetti, P., Hur, M.H., Diebel, M.E., Monville, F., Dutcher, J., et al. (2009). Breast cancer cell lines contain functional cancer stem cells with metastatic capacity and a distinct molecular signature. Cancer Res. *69*, 1302–1313.

Coleman, R.E. (2006). Clinical features of metastatic bone disease and risk of skeletal morbidity. Clin. Cancer Res. *12*, 6243s–6249s.

Coleman, R.E., and Rubens, R.D. (1987). The clinical course of bone metastases from breast cancer. Br. J. Cancer *55*, 61–66.

Coleman, R.E., Smith, P., and Rubens, R.D. (1998). Clinical course and prognostic factors following bone recurrence from breast cancer. Br. J. Cancer *77*, 336–340.

Coleman, R.E., Guise, T.A., Lipton, A., Roodman, G.D., Berenson, J.R., Body, J.J., Boyce, B.F., Calvi, L.M., Hadji, P., McCloskey, E.V., et al. (2008). Advancing treatment for metastatic bone cancer: consensus recommendations from the Second Cambridge Conference. Clin. Cancer Res. *14*, 6387–6395.

Deroose, C.M., De, A., Loening, A.M., Chow, P.L., Ray, P., Chatziioannou, A.F., and Gambhir, S.S. (2007). Multimodality imaging of tumor xenografts and metastases in mice with combined small-animal PET, small-animal CT, and bioluminescence imaging. J. Nucl. Med. *48*, 295–303.

Disibio, G., and French, S.W. (2008). Metastatic patterns of cancers: results from a large autopsy study. Arch. Pathol. Lab. Med. *132*, 931–939.

Echeverria, G.V., Powell, E., Seth, S., Ge, Z., Carugo, A., Bristow, C., Peoples, M., Robinson, F., Qiu, H., Shao, J., et al. (2018). High-resolution clonal mapping of multi-organ metastasis in triple negative breast cancer. Nat. Commun. *9*, 5079.

Esposito, M., Guise, T., and Kang, Y. (2018). The Biology of Bone Metastasis. Cold Spring Harb. Perspect. Med. *8*, a031252.

Gaujoux, R., and Seoighe, C. (2010). A flexible R package for nonnegative matrix factorization. BMC Bioinformatics *11*, 367.

Ghajar, C.M., Peinado, H., Mori, H., Matei, I.R., Evason, K.J., Brazier, H., Almeida, D., Koller, A., Hajjar, K.A., Stainier, D.Y.R., et al. (2013). The perivascular niche regulates breast tumour dormancy. Nat. Cell Biol. *15*, 807–817.

Gonzalez, M.E., Moore, H.M., Li, X., Toy, K.A., Huang, W., Sabel, M.S., Kidwell, K.M., and Kleer, C.G. (2014). EZH2 expands breast stem cells through activation of NOTCH1 signaling. Proc. Natl. Acad. Sci. USA *111*, 3098–3103.

Gundem, G., Van Loo, P., Kremeyer, B., Alexandrov, L.B., Tubio, J.M.C., Papaemmanuil, E., Brewer, D.S., Kallio, H.M.L., Högnäs, G., Annala, M., et al.; ICGC Prostate Group (2015). The evolutionary history of lethal metastatic prostate cancer. Nature *520*, 353–357.

Gupta, P.B., Pastushenko, I., Skibinski, A., Blanpain, C., and Kuperwasser, C. (2019). Phenotypic Plasticity: Driver of Cancer Initiation, Progression, and Therapy Resistance. Cell Stem Cell *24*, 65–78.

Hirukawa, A., Smith, H.W., Zuo, D., Dufour, C.R., Savage, P., Bertos, N., Johnson, R.M., Bui, T., Bourque, G., Basik, M., et al. (2018). Targeting EZH2 reactivates a breast cancer subtype-specific anti-metastatic transcriptional program. Nat. Commun. *9*, 2547.

Hu, J., Al-Ouran, R., Zhang, X., Liu, Z., and Jeong, H.-H. (2020). TraceQC: An R package for quality control of CRISPR lineage tracing data. bioRxiv, doi: 2020.06.05.137141.

Juárez, P., and Guise, T.A. (2011). TGF-β in cancer and bone: implications for treatment of bone metastases. Bone *48*, 23–29.

Kalhor, R., Mali, P., and Church, G.M. (2017). Rapidly evolving homing CRISPR barcodes. Nat. Methods *14*, 195–200.

Kalhor, R., Kalhor, K., Mejia, L., Leeper, K., Graveline, A., Mali, P., and Church, G.M. (2018). Developmental barcoding of whole mouse via homing CRISPR. Science *361*, eaat9804.

Kamran, P., Sereti, K.I., Zhao, P., Ali, S.R., Weissman, I.L., and Ardehali, R. (2013). Parabiosis in mice: a detailed protocol. J. Vis. Exp. (80), 50556.

Kang, Y., Siegel, P.M., Shu, W., Drobnjak, M., Kakonen, S.M., Cordón-Cardo, C., Guise, T.A., and Massagué, J. (2003). A multigenic program mediating breast cancer metastasis to bone. Cancer Cell *3*, 537–549.

Kennecke, H., Yerushalmi, R., Woods, R., Cheang, M.C.U., Voduc, D., Speers, C.H., Nielsen, T.O., and Gelmon, K. (2010). Metastatic behavior of breast cancer subtypes. J. Clin. Oncol. *28*, 3271–3277.

Kim, M.Y., Oskarsson, T., Acharyya, S., Nguyen, D.X., Zhang, X.H.F., Norton, L., and Massagué, J. (2009). Tumor self-seeding by circulating cancer cells. Cell *139*, 1315–1326.

Kingsley, L.A., Fournier, P.G.J., Chirgwin, J.M., and Guise, T.A. (2007). Molecular biology of bone metastasis. Mol. Cancer Ther. *6*, 2609–2617.

Koboldt, D.C., Zhang, Q., Larson, D.E., Shen, D., McLellan, M.D., Lin, L., Miller, C.A., Mardis, E.R., Ding, L., and Wilson, R.K. (2012). VarScan 2: somatic mutation and copy number alteration discovery in cancer by exome sequencing. Genome Res. *22*, 568–576.

Kottakis, F., Polytarchou, C., Foltopoulou, P., Sanidas, I., Kampranis, S.C., and Tsichlis, P.N. (2011). FGF-2 regulates cell proliferation, migration, and angiogenesis through an NDY1/KDM2B-miR-101-EZH2 pathway. Mol. Cell *43*, 285–298.

Ku, S.Y., Rosario, S., Wang, Y., Mu, P., Seshadri, M., Goodrich, Z.W., Goodrich, M.M., Labbé, D.P., Gomez, E.C., Wang, J., et al. (2017). Rb1 and Trp53 cooperate to suppress prostate cancer lineage plasticity, metastasis, and antiandrogen resistance. Science *355*, 78–83.

Li, H., Handsaker, B., Wysoker, A., Fennell, T., Ruan, J., Homer, N., Marth, G., Abecasis, G., and Durbin, R.; 1000 Genome Project Data Processing Subgroup (2009). The Sequence Alignment/Map format and SAMtools. Bioinformatics *25*, 2078–2079.

Lu, C., Han, H.D., Mangala, L.S., Ali-Fehmi, R., Newton, C.S., Ozbun, L., Armaiz-Pena, G.N., Hu, W., Stone, R.L., Munkarah, A., et al. (2010). Regulation of tumor angiogenesis by EZH2. Cancer Cell *18*, 185–197.

Ma, A., Stratikopoulos, E., Park, K.S., Wei, J., Martin, T.C., Yang, X., Schwarz, M., Leshchenko, V., Rialdi, A., Dale, B., et al. (2020). Discovery of a first-in-class EZH2 selective degrader. Nat. Chem. Biol. *16*, 214–222.

Martin, M. (2011). Cutadapt removes adapter sequences from high-throughput sequencing reads. EMBnet. J. *17*, 10.

Minn, A.J., Kang, Y., Serganova, I., Gupta, G.P., Giri, D.D., Doubrovin, M., Ponomarev, V., Gerald, W.L., Blasberg, R., and Massagué, J. (2005). Distinct organ-specific metastatic potential of individual breast cancer cells and primary tumors. J. Clin. Invest. *115*, 44–55.

Nguyen, D.-A., Beeman, N., Lewis, M., Schaack, J., and Neville, M.C. (2000). Intraductal Injection into the Mouse Mammary Gland. In Methods in Mammary Gland Biology and Breast Cancer Research (Springer US), pp. 259–270.

Peinado, H., Zhang, H., Matei, I.R., Costa-Silva, B., Hoshino, A., Rodrigues, G., Psaila, B., Kaplan, R.N., Bromberg, J.F., Kang, Y., et al. (2017). Pre-metastatic niches: organ-specific homes for metastases. Nat. Rev. Cancer *17*, 302–317.

Price, T.T., Burness, M.L., Sivan, A., Warner, M.J., Cheng, R., Lee, C.H., Olivere, L., Comatas, K., Magnani, J., Kim Lyerly, H., et al. (2016). Dormant breast cancer micrometastases reside in specific bone marrow niches that regulate their transit to and from bone. Sci. Transl. Med. *8*, 340ra73.

Sflomos, G., Dormoy, V., Metsalu, T., Jeitziner, R., Battista, L., Scabia, V., Raffoul, W., Delaloye, J.-F., Treboux, A., Fiche, M., et al. (2016). A Preclinical Model for ERα-Positive Breast Cancer Points to the Epithelial Microenvironment as Determinant of Luminal Phenotype and Hormone Response. Cancer Cell *29*, 407–422.

Smid, M., Wang, Y., Zhang, Y., Sieuwerts, A.M., Yu, J., Klijn, J.G., Foekens, J.A., and Martens, J.W. (2008). Subtypes of breast cancer show preferential site of relapse. Cancer Res. *68*, 3108–3114.

Ullah, I., Karthik, G.M., Alkodsi, A., Kjällquist, U., Stålhammar, G., Lövrot, J., Martinez, N.F., Lagergren, J., Hautaniemi, S., Hartman, J., and Bergh, J. (2018). Evolutionary history of metastatic breast cancer reveals minimal seeding from axillary lymph nodes. J. Clin. Invest. *128*, 1355–1370.

Vanharanta, S., and Massagué, J. (2013). Origins of metastatic traits. Cancer Cell *24*, 410–421.

Wang, H., Yu, C., Gao, X., Welte, T., Muscarella, A.M., Tian, L., Zhao, H., Zhao, Z., Du, S., Tao, J., et al. (2015). The osteogenic niche promotes early-stage bone colonization of disseminated breast cancer cells. Cancer Cell *27*, 193–210.

Wang, H., Tian, L., Liu, J., Goldstein, A., Bado, I., Zhang, W., Arenkiel, B.R., Li, Z., Yang, M., Du, S., et al. (2018). The osteogenic niche is a calcium reservoir of bone micrometastases and confers unexpected therapeutic vulnerability. Cancer Cell *34*, 823–839.e7.

Waning, D.L., Mohammad, K.S., Reiken, S., Xie, W., Andersson, D.C., John, S., Chiechi, A., Wright, L.E., Umanskaya, A., Niewolna, M., et al. (2015). Excess TGF-β mediates muscle weakness associated with bone metastases in mice. Nat. Med. *21*, 1262–1271.

Weilbaecher, K.N., Guise, T.A., and McCauley, L.K. (2011). Cancer to bone: a fatal attraction. Nat. Rev. Cancer *11*, 411–425.

Ye, X., and Weinberg, R.A. (2015). Epithelial-Mesenchymal Plasticity: A Central Regulator of Cancer Progression. Trends Cell Biol. *25*, 675–686.

Yu, C., Wang, H., Muscarella, A., Goldstein, A., Zeng, H.C., Bae, Y., Lee, B.H.I., and Zhang, X.H.F. (2016). Intra-iliac artery injection for efficient and selective modeling of microscopic bone metastasis. J. Vis. Exp. *2016*, 1–7.

Yue, Z., Chen, J., Lian, H., Pei, J., Li, Y., Chen, X., Song, S., Xia, J., Zhou, B., Feng, J., et al. (2019). PDGFR-β Signaling Regulates Cardiomyocyte Proliferation and Myocardial Regeneration. Cell Rep. *28*, 966–978.e4.

Zhang, X.H.F., Jin, X., Malladi, S., Zou, Y., Wen, Y.H., Brogi, E., Smid, M., Foekens, J.A., and Massagué, J. (2013). Selection of bone metastasis seeds by mesenchymal signals in the primary tumor stroma. Cell *154*, 1060–1073.

Zhang, L., Yao, J., Wei, Y., Zhou, Z., Li, P., Qu, J., Badu-Nkansah, A., Yuan, X., Huang, Y.W., Fukumura, K., et al. (2020). Blocking immunosuppressive neutrophils deters pY696-EZH2-driven brain metastases. Sci. Transl. Med. *12*, 5387.

STAR★METHODS

KEY RESOURCES TABLE

REAGENT or RESOURCE	SOURCE	IDENTIFIER
Antibodies		
mRFP in 1:500, Rabbit	Rockland	Cat# 600-401-379; RRID: AB_2209751
GFP in 1:500, Chicken	Abcam	Cat# ab13970; RRID: AB_300798
Anti-Mouse CD31 in 1:200, Goat	R&D Systems	Cat# AF3628; RRID: AB_2161028
Anti-Mouse VE-Cadherin in 1:200, Goat	R&D Systems	Cat# AF1002; RRID: AB_2077789
In Vivo Ready Anti-Mouse CD16 / CD32 (2.4G2), 1:100	Tonbo Biosciences	Cat# 40-0161-M001; RRID: AB_2621443
Anti-CD44 Rat Monoclonal Antibody APC, 1:100	Tonbo Biosciences	Cat# 20-0441-U100; RRID: AB_2621572
Anti-ALDH1A1 (B-5) Alexa Fluor 488, 1:100	Santa Cruz Biotechnology	Cat# sc-374149-AF488; RRID: AB_10917910
DsRed Antibody (E-8) Alexa Fluor® 594, 1:100	Santa Cruz Biotechnology	Cat# sc-390909-AF594; RRID: AB_2801575
anti-Chicken IgY, Alexa Fluor 488 in 1:500, Donkey	Jackson ImmunoResearch	Cat#703-546-155; RRID: AB_2340376
anti-Mouse IgG, Alexa Fluor 488 in 1:500, Donkey	Jackson ImmunoResearch	Cat#715-545-151; RRID: AB_2341099
anti-Rat IgG, Alexa Fluor 488 in 1:500, Donkey	Jackson ImmunoResearch	Cat#712-545-153; RRID: AB_2340684
anti-Rabbit IgG, Alexa Fluor 555 in 1:500, Donkey	Thermo Fisher Scientific	Cat# A31572; RRID: AB_162543
anti-Goat IgG, Alexa Fluor 647 in 1:500, Donkey	Jackson ImmunoResearch	Cat# 705-606-147; RRID: AB_2340438
anti-Rabbit IgG, Alexa Fluor 647 in 1:500, Donkey	Jackson ImmunoResearch	Cat# 711-605-152; RRID: AB_2492288
Anti-Mouse CD31, Alexa Fluor 488	R&D Systems	Cat# AF3628G-100
Anti-Cytokeratin 8, Rat, 1:100	DSHB	Cat# TROMA-I; RRID: AB_531826
Anti-Cytokeratin 19, Rat, 1:100	DSHB	Cat# TROMA-III; RRID: AB_2133570
PDGF Receptor β (28E1) Rabbit mAb, 1:1000	Cell Signaling Technology	Cat# 3169S; RRID: AB_2162497
Fgf Receptor 1 (D8E4) XP® Rabbit mAb, 1:1000	Cell Signaling Technology	Cat# 9740S; RRID: AB_11178519
Ezh2 (D2C9) XP® Rabbit mAb, 1:1000 in western blotting, 1:100 in immunofluorescent staining	Cell Signaling Technology	Cat# 5246S; RRID: AB_10694683
HCAM/CD44 rat antibody (IM7), 1:1000	Santa Cruz Biotechnology	Cat# sc-18849; RRID: AB_2074688
γ-catenin Antibody (H-1), 1:1000	Santa Cruz Biotechnology	Cat# sc-8415; RRID: AB_628152
Occludin Antibody (E-5), 1:1000	Santa Cruz Biotechnology	Cat# sc-133256; RRID: AB_2156317
Anti-N Cadherin antibody, 1:200	Abcam	Cat# ab12221; RRID: AB_298943
Anti-human vimentin antibody, 1:2000 in western blotting, 1:200 in immunofluorescent staining	Leica	Cat# VIM-V9-L-CE; RRID: AB_564055
ZEB1 Antibody (H-3), 1:1000	Santa Cruz Biotechnology	Cat# sc-515797
SLUG Antibody (A-7), 1:200	Santa Cruz Biotechnology	Cat# sc-166476; RRID: AB_2191897
GAPDH Antibody (FL-335), 1:1000	Santa Cruz Biotechnology	Cat# sc-25778; RRID: AB_10167668
Goat Anti-Rat IgG Polyclonal Antibody (IRDye® 800CW)	LI-COR Biosciences	Cat# 926-32219; RRID: AB_1850025
Goat Anti-Rabbit IgG Polyclonal Antibody (IRDye® 800CW)	LI-COR Biosciences	Cat# 926-32211; RRID: AB_621843
Goat Anti-Mouse IgG Polyclonal Antibody (IRDye® 800CW)	LI-COR Biosciences	Cat# 926-32210; RRID: AB_621842
Chemicals, peptides, and recombinant proteins		
Dextran, Fluorescein, 70000 MW	Thermo Fisher Scientific	Cat# D1822
EPZ011989	Epizyme	N/A
RapiClear® 1.49	SunJin Lab	Cat# RC149001
Critical commercial assays		
NEBNext® Multiplex Oligos for Illumina	New England BioLabs	Cat# E7600S
NEBNext® Ultra II DNA Library Prep Kit for Illumina	New England BioLabs	Cat# E7645S
Nextseq 500/550 high output v2 kit	Illumina	Cat# 20024908
NEBNext® High-Fidelity 2X PCR Master Mix	New England BioLabs	Cat# M0541S
PlatinumTaq DNA Polymerase	Thermo Fisher Scientific	Cat# 10966026

(*Continued on next page*)

Continued

REAGENT or RESOURCE	SOURCE	IDENTIFIER
Tumor Dissociation Kit, Mouse	Miltenyi Biotec	Cat# 130-396-730
Aldefluor™ Kit	Stemcell Tech	Cat# 01700
Deposited data		
Raw data of Barcode Sequencing	GEO	GSE161145
Raw data of RNA Sequencing of SCP21 cells	GEO	GSE160773
Raw data of WES Sequencing of SCP21 cells	GEO	GSE161181
Experimental models: Cell lines		
Human breast cancer MCF7	ATCC	Cat# HTB-22; RRID: CVCL_0031
Human breast cancer MDA-MB-231	ATCC	Cat# HTB-26; RRID: CVCL_0062
Human prostate cancer PC-3	ATCC	Cat# CRL-1435; RRID: CVCL_0035
Murine breast cancer AT-3	EMD Millipore	Cat# SCC178; RRID: CVCL_VR89
MCF7 Single cell derived population SCP2	This Paper	N/A
MDA-MB-231 Single cell derived population SCP21	This Paper	N/A
Experimental models: Organisms/strains		
Mouse: Hsd:Athymic Nude-Foxn1^{nu}	Envigo	N/A
Mouse: C57BL/6J	Jackson Laboratories	RRID: IMSR_JAX:000664
Mouse: NOD.Cg-Rag1tm1Mom Il2rgtm1Wjl/SzJ	Jackson Laboratories	RRID: IMSR_JAX:007799
Oligonucleotides		
Primers for CD44, GAPDH, ZEB1, CDH1, FN1, CDH2, VIM, EZH2, SNAI2, GJA1, and JUP mRNA, see Table S2	This Paper	N/A
Primers for human HPRT1 and mouse Gapdh DNA, see Table S2	This Paper	N/A
Oligonucleotides for cloning of TLCV2-A26, see Table S2	This Paper	N/A
Primers for library preparation of barcodes, see Table S2	This Paper	N/A
shRNA targeting sequence: EZH2 #1: TTACTGTCCCAATGGTCAG	Horizon Discovery	Cat# RHS4696-200690448
shRNA targeting sequence: EZH2 #2: TTTGGCTTCATCTTTATTG	Horizon Discovery	Cat# RHS4696-200688725
Recombinant DNA		
pwpt-Fluc/GFP or pwpt-Fluc/RFP	Wang et al., 2015	NA
TLCV2	Barger et al., 2019	Addgene #87360
TRIPZ-shEZH2-1	Horizon Discovery	Cat# RHS4696-200690448
TRIPZ-shEZH2-2	Horizon Discovery	Cat# RHS4696-200688725
Software and algorithms		
ImageJ	National Institute of Health	https://imagej.nih.gov/ij/
Living Image	PerkinElmer	https://www.perkinelmer.com:443/product/spectrum-200-living-image-v4series-1-128113?c=true&NC=USA
Inveon Research Workplace	SIEMENS	http://www.siemens-healthineers.com/en-us/molecular-imaging/preclinical-imaging/inveon-workplace/
Inkscape	The Inkscape Project	https://inkscape.org/
R 3.3.4	R Core Team	https://rstudio.com/
Graphpad Prism 8	GraphPad Software, Inc.	https://www.graphpad.com/scientific-software/prism/
FlowJo, v10.0	BD	https://www.flowjo.com/
Imaris Viewer	Oxford Instrument	https://imaris.oxinst.com/imaris-viewer
TraceQC	(Hu et al., 2020)	https://github.com/LiuzLab/TraceQC

(*Continued on next page*)

Continued

REAGENT or RESOURCE	SOURCE	IDENTIFIER
Cutadapt	Martin, 2011	https://github.com/marcelm/cutadapt/
Trim Galore	Felix Krueger	https://github.com/FelixKrueger/TrimGalore
SAMtools	Li et al., 2009	http://www.htslib.org/
Picard	Broad Institute	http://broadinstitute.github.io/picard/
VarScan2	Koboldt et al., 2012	http://dkoboldt.github.io/varscan/
Expands	Andor et al., 2014	http://cran.r-project.org/web/packages/expands
Other		
Barcode Analysis Code	This paper	https://github.com/LiuzLab/CRISPR_bone_metastasis-manuscript

RESOURCE AVAILABILITY

Lead contact

Further information and requests for resources or reagents should be directed to the lead contact Dr. Xiang H.-F. Zhang (xiangz@bcm.edu).

Materials availability

Plasmids and cells generated in this study are available upon requests with a completed Materials Transfer Agreement (MTA). There are restrictions to the availability of EPZ011989 due to the restriction of MTA with Epizyme.

Data and code availability

The raw data of mRNA sequencing, WES sequencing and barcode sequencing are available in NIH Gene Expression Omnibus with the accession number GEO: GSE160773, GSE161181 and GSE161145. The reference series GEO: GSE161146 links all the datasets. The TraceQC package can be found at https://github.com/LiuzLab/TraceQC. The code for the NMF analysis of barcodes can be found at https://github.com/LiuzLab/CRISPR_bone_metastasis-manuscript.

EXPERIMENTAL MODEL AND SUBJECT DETAILS

Cell lines and Cell Culture

Human triple negative breast cancer cell lines MDA-MB-231(RRID: CVCL_0062), human estrogen receptor positive luminal breast cancer cell line MCF7 (RRID: CVCL_0031), human prostate cancer cell line PC-3 (RRID: CVCL_0035), and HEK293T cells (RRID: CVCL_0063) were obtained from ATCC. AT-3 cells (RRID: CVCL_VR89) was a gift from Dr. Scott Abrams at Roswell Park Cancer Center. SCP21 cells were from Joan Massagué lab. MCF7 SCPs were generated from single cells of parental MCF7 cells in the lab. All cells were maintained in DMEM high glucose media supplemented with 10% FBS and 1% penicillin-streptomycin in 5% CO_2 37°C incubator. MCF7, MDA-MB-231 and their derivative cells were authenticated by the Cytogenetics and Cell Authentication Core at MD Anderson Cancer Center by STR profiling. The mycoplasma contamination was routinely examined in the lab using PlasmoTest Mycoplasma Detection Kit (InvivoGen) and no contamination was detected in the cells used in this study. Incucyte (Essen BioScience) was used to assess the cell growth in culture.

Animals

The *in vivo* studies were covered by and conducted in accordance with a protocol approved by the Baylor College of Medicine Institutional Animal Care and Use Committee. Nude mice [Athymic Nude-Foxn1^{nu}] were purchased from Envigo, while female C57BL/6J (RRID: IMSR_JAX:000664) and immunodeficient NOD.Cg-Rag1tm1Mom Il2rgtm1Wjl/SzJ (RRID: IMSR_JAX:007799) mice were from Jackson Laboratories. Age-matched female or male mice of 6- to 8-week-old were used for breast cancer cells, or prostate cancer cells, respectively. In tumor models using MCF7 and MCF7-SCP2 cells, slow-released estradiol tubes were implanted under the dorsal neck skin of animals one week prior the tumor implantation. 2 weeks after arrival, mice were randomly allocated to experimental groups.

METHOD DETAILS

Plasmid Construction

TLCV2 plasmid was a gift from Adam Karpf (Addgene plasmid # 87360) (Barger et al., 2019). To construct the TLCV2-hgRNA-A26 plasmid, the synthesized hgRNA-A26 oligos were annealed and ligated with BsmBI and EcoRI digested TLCV2 plasmid. The TRIPZ

inducible EZH2 shRNA plasmids (Clone ID: V2THS_63066 and V2THS_63067) were purchased from Horizon Discovery Ltd. Plasmids were extracted from the growing bacterial clones and confirmed by Sanger sequencing. The oligo sequences are listed in the Table S2.

Lentiviral Production and Transduction

Luciferase/fluorescent protein reporter plasmids, or TRIPZ-shEZH2, or TLCV2-hgRNA-A26 were transfected together with psPAX2 and pMD2.G packaging plasmids into HEK293T cells using X-tremeGENE HP DNA transfection reagent (Sigma). 48 hours later, the supernatant was harvested and filtered by 0.45 um filter (VWR International). Cancer cells were transduced by the fresh lentivirus together with 8ug/ml polybrene (Sigma). Two days later, GFP or mRFP positive cells were sorted to generate reporter cell lines. For cells with inducible evolving barcodes or shEZH2, cells were selected with 2 μg/ml puromycin for 10 days before experiments.

In vitro activation of hgRNA barcodes

5E5 barcoded MDA-MB-231 cells were seeded on the 10-cm dish and the next day treated with 100 μg/ml doxycycline for 2 hours. Cells were then rinsed by PBS three times to completely remove doxycycline and then allowed to grow *in vitro* for 4 days. 1 million cells were collected for barcode sequencing and 0.5 million cells were re-cultured and received next round of doxycycline treatment 24 hours later.

Intra-iliac artery and Intra-iliac vein Injection

Both intra-iliac artery and vein injections were performed as previously described (Yu et al., 2016). Briefly, animals were anesthetized and restrained on a warming pad. The surgery area was sterilized, and a 7-8 mm incision was made between the right hind limb and abdomen to expose the common iliac vessels. Cancer cells were suspended in 100 μL PBS and injected to the iliac artery or vein by 31G insulin syringe (Becton Dickinson) to generate bone or lung metastases, respectively. For inducible knockdown of EZH2 *in vivo*, animals were randomly separated into two groups, and given 0.2 mg/ml doxycycline in 1% sucrose water or vehicle for 7 weeks one week after the injection, respectively.

Intra-femoral and Intra-Cardiac Injection

For intra-femoral injection, a port through the right femoral plateau was made by a 28G syringe needle into the bone marrow cavity. Then, cancer cells in 20 μL PBS was slowly delivered into the bone marrow cavity through the port. The syringe was then hold for about 20 s to allow the equilibrium of bone marrow before retrieval. For intra-cardiac injection, cancer cells in 100 μL PBS were directly injected into the left ventricle of anesthetized animals using 26G syringe.

Mammary Fat Pad and Intra-Ductal Injection

For mammary tumor models, cancer cells mixed 1:1 with growth factor reduced Matrigel Matrix (Corning) were orthotopically implanted into the fourth mammary fat pad of mice. In the cross-seeding experiment, the mammary tumors were implanted on the opposite side of mammary fat pad immediately after the IIA injection of same number of cancer cells in the right hind limb on the same animal. The intra-ductal injection (or MIND model) was performed as previously reported (Nguyen et al., 2000). Briefly, the tip of the fourth nipples was cut off and cancer cells in 10 ul PBS were directly injected into the exposed duct using 30G blunt needle fitted to a Hamilton syringe.

Parabiosis and Reverse Procedure

The procedure for parabiosis and reverse procedure were described previously (Kamran et al., 2013). Mice were housed in pairs for at least two weeks to ensure the harmonious cohabitation before the surgery. The donor mice were given a tumor implantation surgery on the right side of the body via MFP or IIA injection one week before the parabiosis surgery. During parabiosis surgery, both donor and recipient mice were anesthetized by isoflurane and placed back to back on a warming pad. A longitudinal incision was made on the left side of donor mice and right side of recipient mice starting from the elbow to the knee joints, and then the skin was gently detached from the subcutaneous fascia. The joints between parabiotic pairs were tightly connected with non-absorbable 4-0 suture. The skin incision was then closed side-by-side with absorbable 5-0 suture. The parabiotic pairs were closely monitored until full recovery. 7 weeks after the surgery, a reverse procedure was performed to separate the parabiotic pairs. The recipient mice were then continuously monitored with bioluminescent imaging bi-weekly till the detection of metastatic lesions or up-to 4 months.

In vivo activation of hgRNA barcodes

1E5 barcoded MDA-MB-231 or AT-3 cells were implanted in nude or C57BL/6 mice respectively to form mammary tumors. For MDA-MB-231 cells, 5 weeks later, the mammary tumors were completely removed, and a single dose of 5mg/kg doxycycline was then applied to the animals via I.P. injection weekly for 5 weeks. At week 12, tissues with metastatic MDA-MB-231 lesions were dissected and subjected to further analysis. The AT-3 tumors were resected 18 days after implantation, and mice were given a dose of 5mg/kg doxycycline via I.P. injection weekly. The metastatic tissues of AT-3 cells were dissected at day 42 after tumor implantation.

Bioluminescence Imaging and Tissue Collection

In vivo bioluminescence imaging (BLI) was performed weekly with IVIS Lumina II (Advanced Molecular Vision). Briefly, the anesthetized animals were imaged immediately after administration of 100 μL 15 mg/ml D-luciferin (Goldbio) via retro-orbital venous sinus. To ease the comparison across different animals and tissues, the exposure setting was fixed in this study except that the duration of exposure was adjusted to avoid saturation of signals. If not specified, all the animals were sacrificed 8 weeks after the tumor engraftment. At the end point, live animals were given D-Luciferin and immediately dissected. The tissues were examined by *ex vivo* BLI imaging following a fixed order. The whole process of dissection and *ex vivo* imaging was typically done in less than 15 minutes for each animal. The excised tissues were either snap frozen immediately or fixed by 4% PFA at 4°C overnight, cryopreserved with 30% sucrose PBS solution, and then embedded in OCT (Tissue-Tek). For bone tissues, a 7-day decalcification in 14% PH 7.4 EDTA solution was required before embedding. To quantify the metastatic burden, the total BLI flux was calculated over the same region of interest defined specifically for each type of tissues using Living Image software (PerkinElmer) and presented as total count/s to normalize the influence of exposure duration. The status of 'multi-site metastases' refers to the metastatic involvement of at least 3 tissues other than the primary site of implantation (IIA or IF, right hindlimb; IIV, lung; MFP or MIND, mammary gland). Metastatic lesions were defined as the clustered, normally distributed bioluminescent signals above the threshold of 15 counts/pixel under the maximum 120 s exposure.

Small Animal PET-CT Scanning

PET-CT scanning on tumor bearing mice was performed by the Small Animal Imaging Facility (SAIF) core at Texas Children Hospital. Briefly, animals were fasted for about 12 hours and given with Flourine-18 labeled fluorodeoxyglucose (18F-FDG) one hour before the scanning via intra-peritoneal injection (Cyclotope, Houston, TX). The scanning was performed with appropriate anesthesia and monitoring to maintain normal breathing rates of subjects. Images were acquired by an Inveon scanner (Siemens AG, Knoxville, TN). 220 CT scan projections were acquired with 290 ms exposure under 60 kVp X-ray tube voltage and 500 μA current, followed by a 30-minute PET scan. The PET scans were then reconstructed and corrected with CT scans using OSEM3D method. A thresholding of 90% of SUVmax was applied to the PET images to indicate the tumors.

Deep Imaging of Intact Tissues

Animals with metastases were retro-orbitally given 1mg 70kDa fluorescein-dextran (Invitrogen) and 10mg Alexa Fluor 488 conjugated anti-mouse CD31 antibody (R&D System) to label vasculatures. 10 minutes afterward, tissues with metastatic lesions were excised guiding by *ex vivo* BLI imaging. The dissected tissues were then cleaned with cold PBS and fixed in 4% PFA for 4 hours at 4°C. To create the window for deep imaging, part of the cortical bones was gently peeled off. Bone tissues were then decalcified at 4°C overnight with constantly shaking. Then, tissues were equilibrated in 30% sucrose solution and later in RapiClear® 1.49 (SunJin Lab Co) overnight until the tissues became transparent. The cleared tissues were mounted with RapiClear® 1.49 and Z stack imaging was performed with a Fluoview FV2000MPE microscope (Olympus). The vasculatures and tumor lesions were reconstructed with Imaris Viewer (Oxford Instrument).

Immunofluorescent Staining

Frozen sections and HE-stained slides were prepared by the Breast Center Pathology Core at Baylor College of Medicine. The immunofluorescent staining was performed with antibodies against mRFP (Rockland, 600-401-379), EGFP (Abcam, 13970), mouse CD31 (R&D Systems, AF3628), and mouse VE-Cadherin (R&D Systems, AF1002). Briefly, the frozen slides were warmed at room temperature for 10 minutes and rinsed with PBS twice. 50mM Ammonium chloride in PBS were applied to the slides to reduce the autofluorescence. Then the sections were penetrated with 0.3% Triton X-100 in PBS for 30 minutes and blocked by 10% donkey serum in PBS-GT (2% Gelatin, 0.1% Triton X-100) for 1 hour at RT. Sections were then incubated with primary antibodies overnight at 4°C. The next day, after PBS washing for three times, the slides were incubated with Alexa Fluor 488 conjugated Donkey anti-Chicken IgY (Jackson ImmunoResearch, 703-546-155), Alexa Fluor 555 conjugated Donkey anti-Rabbit IgG (Thermo Fisher, A31572), and Alexa Fluor 647 conjugated Donkey anti-Goat IgG (Jackson ImmunoResearch, 705-606-147) for 2 hours at RT. The stained sections were then washed, and mounted with ProLong™ Gold antifade mountant with DAPI (Thermo Fisher, P36935). Images were acquired by a Zeiss LSM780 confocal microscope, or a Leica DMi8 inverted microscope, or a Zeiss Axioscal.Z1 scanner. Immunofluorescent images were first exported by ZEN (Zeiss), or LAS X (Leica Microsystem). The exported images were then analyzed and quantified by Fiji.

Genomic DNA Extraction from Tissues and Cells

The spatially isolated metastatic lesions were excised and separated with the guide of BLI imaging. The tools were cleaned with 70% isopropanol followed by a bead-sterilizer in between different collections to avoid cross-contamination. The dissected tissues were snap-frozen and stored in −80°C freezer until next step. Samples were then homogenized with lysis buffer from Quick-DNA Miniprep Plus Kit (Zymo Research, D4068) by Precellys Lysing Kit (Bertin Instruments, CK14 or MK28-R) on a Precellys Evolution homogenizer (Bertin Instruments). Then, the homogenized tissues or cells were incubated at 55°C for 3 h and treated with 0.33 mg/mL RNase A at 37°C for 15 min. Genomic DNA was further extracted using Quick-DNA Miniprep Plus Kit. The final product was assessed by NanoDrop 2000 (Thermo Scientific) and 100 ng DNA from each sample was used in q-PCR to determine the human/mouse DNA ratio

with primers specifically targeting human HPRT and mouse Gapdh gene. For the samples do not reach the threshold at the end of 40 cycles of PCR, a Ct value of 40 cycles was assigned for the calculation of human DNA ratio.

Amplification and Sequencing of hgRNA Barcodes

Barcodes were amplified by two rounds of PCR. The first round of PCR was performed with 100 ng genomic DNA using Platinum Taq DNA Polymerase (Invitrogen) with Barcode-For and Barcode-Rev primers in 15 cycles. The second round of PCR were performed in a real-time setting and stopped in mid-exponential phase using PowerUp SYBR Green Master Mix (Thermo Fisher) with Barcode-P5-For and Barcode-P7-Rev primers. The sequences of primers are provided in Key resources table. PCR products were then column-purified with QIAquick PCR purification Kit (QIAGEN) and assessed with Qubit. The NEBNext Multiplex oligos for Illumina (Dual index primer set 1,NEB, E7600S) and the NEB library preparation kit for Illumina (NEB, #E7645S) were used for library preparation as previously described (Kalhor et al., 2017). Barcodes from MDA-MB-231 spontaneous metastases were sequenced on Illumina Hiseq lanes provided by Novogene while other samples were sequenced with NextSeq 500/550 lanes by the Genomic and RNA profiling Core at Baylor College of Medicine.

Evolving Barcode Data Processing

A customized pipeline was used to extract the sequences and counts of barcodes from FASTQ files. Briefly, to identify the barcoding region, the R1 sequence was globally aligned to the A26 reference barcode. The parameters used for alignment are: +2 for match score, −2 for mismatch score, −6 for gap opening penalty and −0.1 for gap extension penalty. Next, the adaptor sequences were trimmed off from the annotated sequence. Then, the sequences with alignment scores lower than 200 or with count less than 10 were removed from the subsequent analysis. Barcode sequence from each read was extract, which is 117 bps starting from 58 bp before the predicted TSS of TLCV2 plasmid. Then the mutation events were categorized by TraceQC package (https://github.com/LiuzLab/TraceQC) into 4 attributes of barcodes: type of mutations, starting position, length of mutation, and the mutant sequence. The mutation events were normalized by the read count per million (RPM) approach and the normalized count was used to generate the feature matrixes for metastases in each animal. The Shannon entropy of mutation events were calculated using the formula: $H(X) = -\sum_{i=1}^{n} P(x_i)\log_2 P(x_i)$.

Non-negative matrix factorization analysis

To delineate the phylogenetic relation across metastases of different sites, we performed the Non-negative matrix factorization (NMF) analysis on the normalized mutation count matrix using NMF package in R (Gaujoux and Seoighe, 2010). The NMF analysis generate robust clusters on both mutation events and metastatic samples, which can be further interpreted into features shared across clonotypes. Given the dimension of the mutation count matrix, we ran the NMF analysis 200 times to perform the rank survey. To determine the appropriate rank (k) for NMF analysis, in addition to visually examination of the clusters, Cophenetic and Silhouette scores were used to quantitatively evaluate the robustness of NMF clusters. The Cophenetic score measures the similarity of two objects to be clustered into one cluster in the consensus matrix. High Cophenetic correlation means the consensus matrix possesses better separated clusters. In mouse 510, k = 6, while in mouse 509, k = 7 or 8; in mouse 121 and 520, k < 5, is the local optimum as shown in the Cophenetic score curve. The Silhouette score was then used to validate the choice of k, as it indicates the similarity of an object to its belonged cluster. The Silhouette scores also evaluate the consistency between the consensus map and the coefficient matrix. Based on the Silhouette curves, k = 6 in mouse 510 while k = 7 for mouse 509, k = 3 for both mouse 121 and 520 is the local optimum for the consensus matrix in NMF analysis of individual mutation matrix. To enable the reproducibility of the NMF analysis, the final factorization was run with an initial seed on the chosen rank. The body maps were then generated from the values of each basis in a specific metastasis in the mixture coefficient matrix in combination with the value of Shannon entropy. To illustrate the composition flow of barcodes across samples, the count matrix of mutation events was first ranked and segmented to enable the most connectivity between two samples by Excel. The difference of Shannon entropy was used to decide the direction of flow. Chord diagrams were generated by Inkscape to proportionally reflect the flow of mutation events. Bar length indicates the entropy. Solid proportion, mutation events pre-existed in the primary tumor; striped proportion, mutation events induced by doxycycline. The numbers of mutation events are denoted. Connections with the break are mutation events that are absent in the parental lesions but present in primary tumors.

Assessment of Metastasis of Organ-entrained SCPs

SCP21 or MCF7-SCP2 cells tagged with mRFP and luciferase gene were implanted to the mammary fat pads, hind limbs, or lungs of female nude mice through MFP, IIA or IIV injection, respectively. 6 weeks later, 4 mammary, 3 lung and 4 bone entrained cells were recovered from SCP21 xenografts. For MCF7-SCP2 cells, two mammary tumors and one bone metastases were recovered. All the animals failed to develop lung metastases after receiving one million MCF7-SCP2 cells through tail vein injection, therefore lung-entrained MCF7-SCP2 cells were not examined in this study. mRFP+ tumor cells were then sorted out from the single cell mixture prepared by the tumor dissociation kit (Miltenyi Biotec). For bone metastases, bone marrow was discarded, and the bone fragments were subjected to the collagenase digestion prior the tumor dissociation. The organ-entrained cells were then expanded under

regular culture condition, and cryopreserved immediately after reaching confluency, and considered as P1 SCPs. If not specified, cells were sub-cultured every 5 days and most experiments were performed with SCPs at passage 3. The *in vitro* treatment of EPZ011989 (1uM) was started with BoM-SCPs at passage 2 and lasted for 5 days. 1E5 different organ entrained cells (randomly selected) at passage 3 and parental SCP21 cells were injected into the left ventricle (intra-cardiac injection) of nude mice. The animals were monitored by BLI imaging weekly.

Flow Cytometry

Cells were trypsinated at about 80% confluence and the cell number was counted. 20E4 cells were resuspended in 1 mL ALDEFUOR™ Assay buffer, and 5 ul of activated substrate was added into the cell suspension. Then, 0.5 mL of the mixture was transferred to another tube with 5 ul DEAB to inactivate the ALDH enzymatic reaction. Both the DEAB and test samples were incubated at 37°C for 45 min. For CD44 staining, cells were blocked with mouse anti-CD16/32 antibody (Tonbo Biosciences) for 10 minutes and then stained with APC conjugated CD44 antibody (Tonbo Biosciences) on ice for 30 minutes. ALDH+ cells and CD44 expression were then examined with BD LSR Fortessa Analyzer, and analyzed with FlowJo v10.0 (BD). The percentage of ALDH1+ population in test samples was determined with the same gate containing 0.1% positive cells in the corresponding DEAB sample.

RNA and Protein Extraction and Quantification

Total RNA was extracted from TRIzol (Invitrogen) lysed cells by Direct-zol RNA miniPrep Kit (Zymo Research) with an extra step of in-column DNase treatment. For qRT-PCR, cDNA was generated with RevertAid First Strand cDNA synthesis Kit (Thermo Scientific, K1622) with 1 ug of total RNA following the manufacturer's instructions. Real-time PCR was performed with PowerUp SYBR Green Master Mix (Thermo Fisher) on Biorad CFX Real-Time system. The expression levels of GAPDH mRNA were used as the internal control. The primer sequences are listed in the Table S2. For western blotting, cells were directly scratched from the culture dishes and lysed with RIPA buffer. 20 μg of total proteins were used for electrophoresis with NuPAGE® Novex® Gel system (Invitrogen). Proteins were then transferred to a nitrocellulose membrane using iBlot Transfer System (Invitrogen). The membrane was blocked with 5% BSA and incubated with primary antibodies overnight at 4°C. The next day, membranes were incubated with secondary antibodies (LI-COR Bioscience) and scanned by the Odyssey® infrared imaging system. The antibodies and conditions used in this study were listed in Key resources table.

RNA-Sequencing and Whole Exome Sequencing

mRNA sequencing, read mapping, normalization and quantification were performed by Novogene. One of four MFP-SCP21 samples failed the quality check and was excluded from the subsequent analysis. EZH2 signature were calculated as the average expression of EZH2-suppressed genes (MSigDB geneset: LU_EZH2_TARGETS_DN) (Lu et al., 2010). Whole exome sequencing was performed by the Genomic and RNA profiling Core at Baylor College of Medicine with 100X coverage. Sequences were trimmed by Cutadapt (Martin, 2011) and Trim Galore and aligned to hg19 reference genome using the BWA-MEM algorithm after the quality check by FastQC and MultiQC. SAMtools (Li et al., 2009) and Picard (http://broadinstitute.github.io/picard/) were then used to filter the BAM files and remove duplicated reads. The control sample was from 1000-Genomes (ERR031938) and processed accordingly. Copy number and somatic variations were then analyzed with VarScan 2 (Koboldt et al., 2012). The variants with p value less than 0.01 were subjected to the following analyses and processed on Galaxy platform (Afgan et al., 2018). The EXPANDS package (http://cran.r-project.org/web/packages/expands) was used to delineate the clonal structure of SCP21 sublines as previously described (Andor et al., 2014).

Capture and Staining of CTCs

500 μL blood were draw from the right ventricle of anesthetized NRG mice inoculated with mammary tumors or bone metastases after 6 weeks. Blood samples were immediately mixed with 8 mL of red blood cell lysis buffer and incubated on ice for 10 minutes. Samples were then centrifuged at 250 g for 10 minutes at 4°C and the supernatant was discarded. The same steps were repeated once to completely remove red blood cells. Cell pellets were then re-suspended with cold PBS and transferred to poly-L-lysine coated slides. The slides were placed in the 37°C incubator for 30 minutes, and fixed with 4% PFA for 10 minutes. Fixed cells were rinsed with PBS for three times, and permeated with 0.3% Triton X-100 for 30 minutes at RT. Slides were then blocked with donkey serum (Sigma) and anti-mouse CD16/32 antibody (Tonbo Biosciences) for 2 hours and incubated with fluorescence conjugated primary antibodies at 4°C overnight. The next day, slides were stained with DAPI and mounted with Prolong Diamond Antifade Mountant (Molecular Probe). Circulating tumor cells were identified and imaged by a CyteFinder® instrument (Rarecyte) with same exposure setting.

QUANTIFICATION AND STATISTICAL ANALYSIS

Number of animals or independent replicates, and the type of statistical test used are denoted in the figure legends or figures. In most animal experiments, the investigators were not blind to the allocation of animals due to the nature of the experimental design and the need of continual monitoring on subjects. All the *in vitro* study has been repeated at least twice with more than three independent replicates, and the investigators were blind until the assessment of outcome. Sample sizes were chosen

empirically or based on the preliminary experiments, and no statistical approach was used to pre-determine the group size. If not specified otherwise, all the data and statistical analysis were generated by GraphPad Prism 8. Graphs generally show all replicate values. In bar and curve plots, data are represented as Mean ± SEM. Some data points were accidentally not saved during the BLI imaging and therefore missing in Figures 1J, 2C, and 2G. Only part of the animals in Figure 5A were examined after dissection due to the institutional lockdown during the pandemic. All the other available data points were included and two-sided tests were performed in the analysis. F test was performed prior to the Student's t test to assess the variance difference. Welch's correction was applied to the Student's t test if the null hypothesis of F test was rejected. $p < 0.05$ were considered as statistically significant.

Supplemental figures

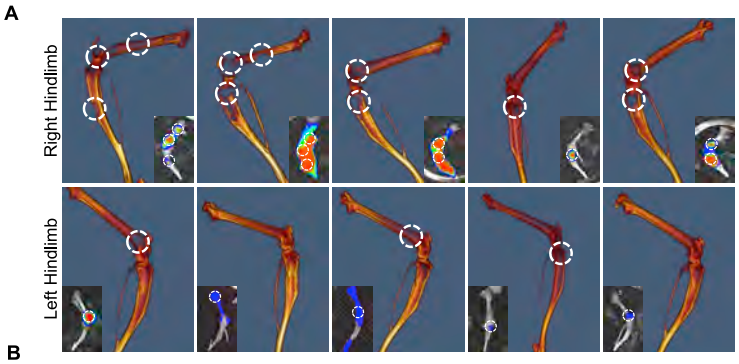

BLI \ μCT	Yes	No
Yes	23	12
No	0	-

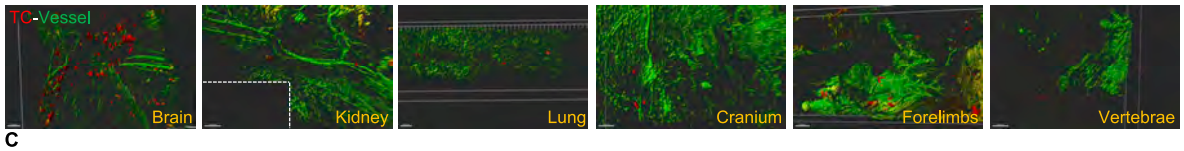

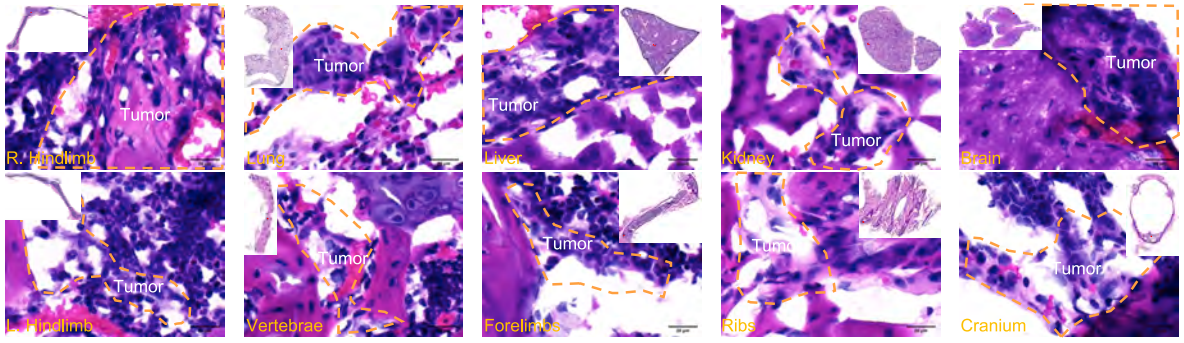

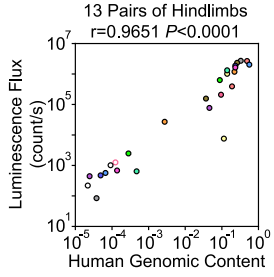

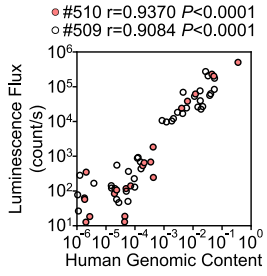

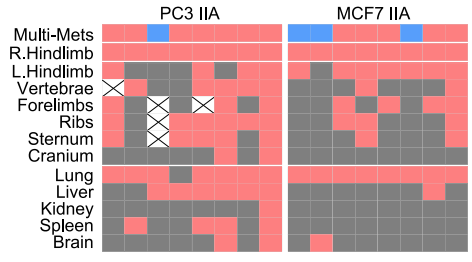

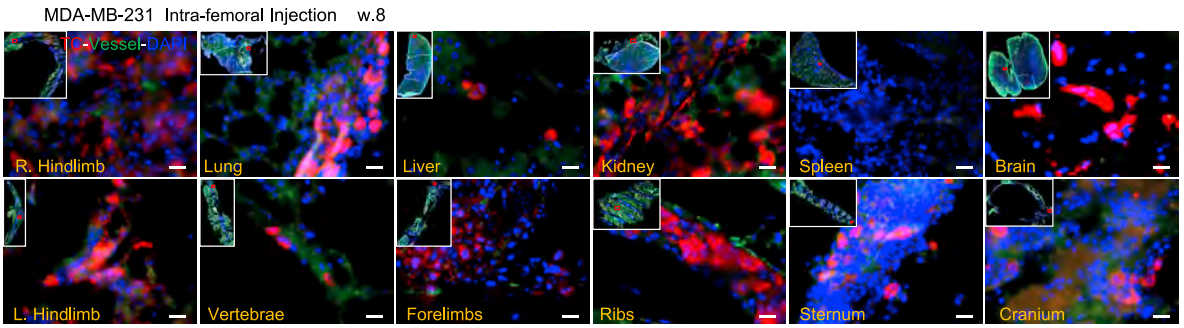

(legend on next page)

Figure S1. Metastatic spread in animals with established bone metastases, related to Figure 1

(A) Metastatic lesions detected by microCT and the corresponding *ex vivo* bioluminescent imaging (lower) on the same bones. Right table showing that 12 in 35 lesions recovered by BLI were not detected by microCT in this study.

(B) Deep imaging of metastases in various tissues from mice with primary bone metastases at the right hindlimb. Clarified tissues were imaged in tiles. The obtained image tiles were then stitched by Fluoview to reconstruct views of vasculatures and tumor lesions by Imaris Viewer. The dotted box indicates a part of image that was not appropriately scanned and stitched due to lack of focus. Scale bar, 100 μm.

(C) H&E staining of tumor lesions across various tissues from mice with IIA-injected bone metastases. Scale bar, 20 μm.

(D-E) Correlation plots showing the relationship between *ex vivo* BLI intensities and the lesion size across paired hindlimbs (D) or various tissues (E). The lesion size refers to the ratio of human genomic content on tissues of the same weight here. Such ratio was calculated with the Ct values of human HPRT and mouse Gapdh DNA by q-PCR. Spearman correlation r and p values were indicated.

(F) Heatmap showing the metastatic pattern in animals with established PC3 or MCF7 bone lesions via IIA injection. Red cells indicate the presence while gray cells represent the absence of detectable lesions by *ex vivo* BLI imaging. n (# of mice) = 8 (PC3); 8 (MCF7).

(G) Representative immunofluorescent images of tumor lesions in skeletal and other tissues from animals with intra-femoral injected MDA-MB-231 cells. To obtain complete views of entire organs, smaller fields were acquired in tiles by mosaic scanning and then stitched by Zen. Scale bar, 20 μm.

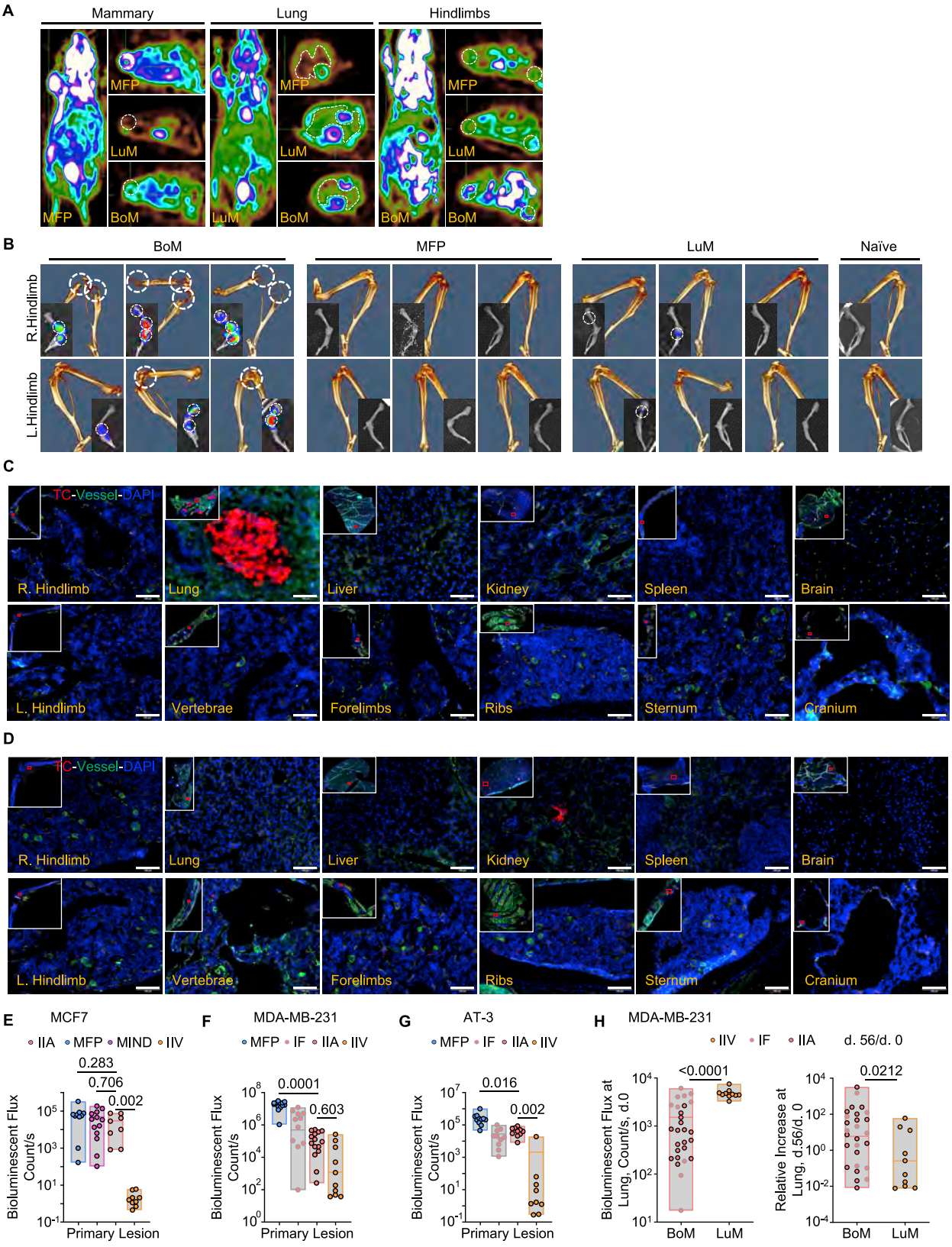

(legend on next page)

Figure S2. Established bone tumors metastasize more to other tissues, related to Figure 2

(A) PET scanning of mammary gland, lung, and hindlimbs of animals with established mammary tumors (MFP), lung metastases (LuM) or bone metastases (BoM).

(B) microCT scanning of the hindlimbs from mice with established mammary tumors, lung metastases, or bone metastases and tumor-free control mice.

(C-D) Representative immunofluorescent images of tissues from mice with lung metastases (C) or mammary tumors (D). To obtain complete views of entire organs, smaller fields were acquired in tiles by mosaic scanning and then stitched by Zen. Scale bar, 100 μm.

(E-G) Combined bar plot and dot plot showing the tumor burden of primary lesions in different models of MCF7 (E), MDA-MB-231 (F) and AT-3 (G) cells. The primary lesions refer to the mammary tumors in MFP models, right hindlimb bone metastases in IIA and IF models, and lung metastases in IIV models.

(H) Combined bar plot and dot plot showing the initial tumor burden at lung after injection (d. 0, Left) and the normalized increase of lung tumor burden at the end point (d. 56, Right) in mice with bone or lung metastases.

p values were determined by Dunn's test following Kruskal-Wallis test in (E), (F) and (G); by Mann-Whitney test in (H).

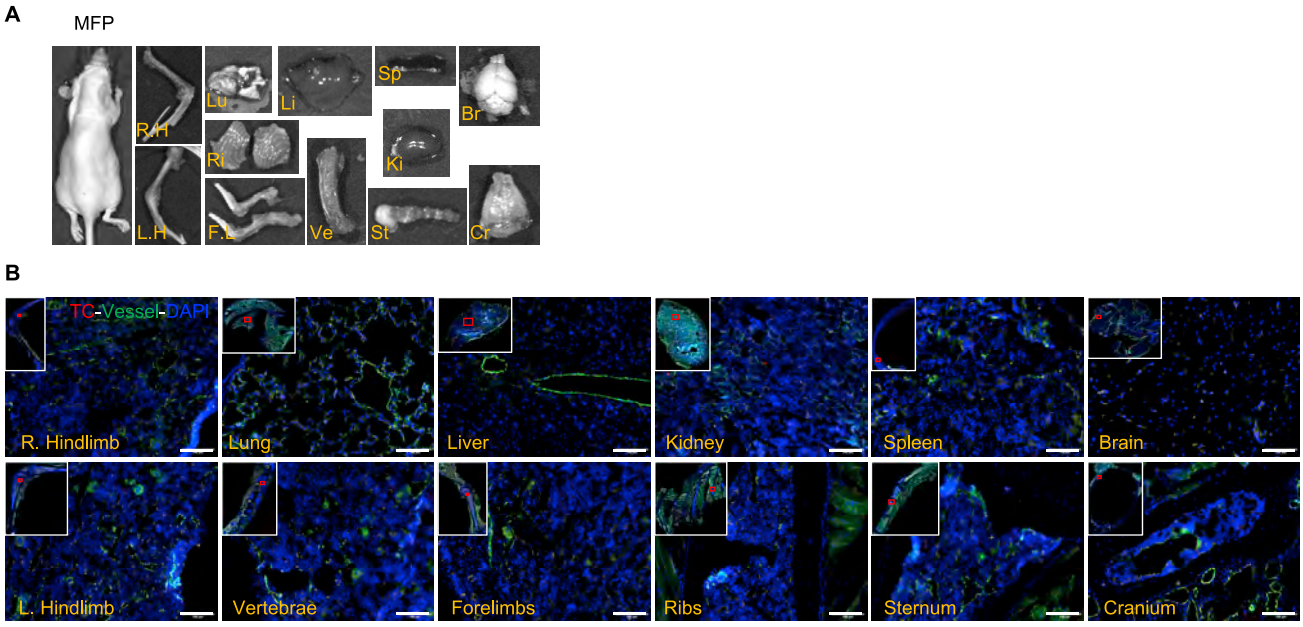

Figure S3. Recipient mice parabiotic with mammary tumor-bearing mice were tumor-free, related to Figure 3

(A) Representative *ex vivo* BLI images of tissues from recipient mice in mammary tumor group, in comparison to Figure 3E. 19 animals in total were examined. (B) Representative immunofluorescent images of various tissues from recipient mice parabiotic with mammary tumor bearing mice, in comparison to Figure 3G. Tissues from 8 animals were examined. To obtain complete views of entire organs, smaller fields were acquired in tiles by mosaic scanning and then stitched by Zen. Scale bar, 100 μm.

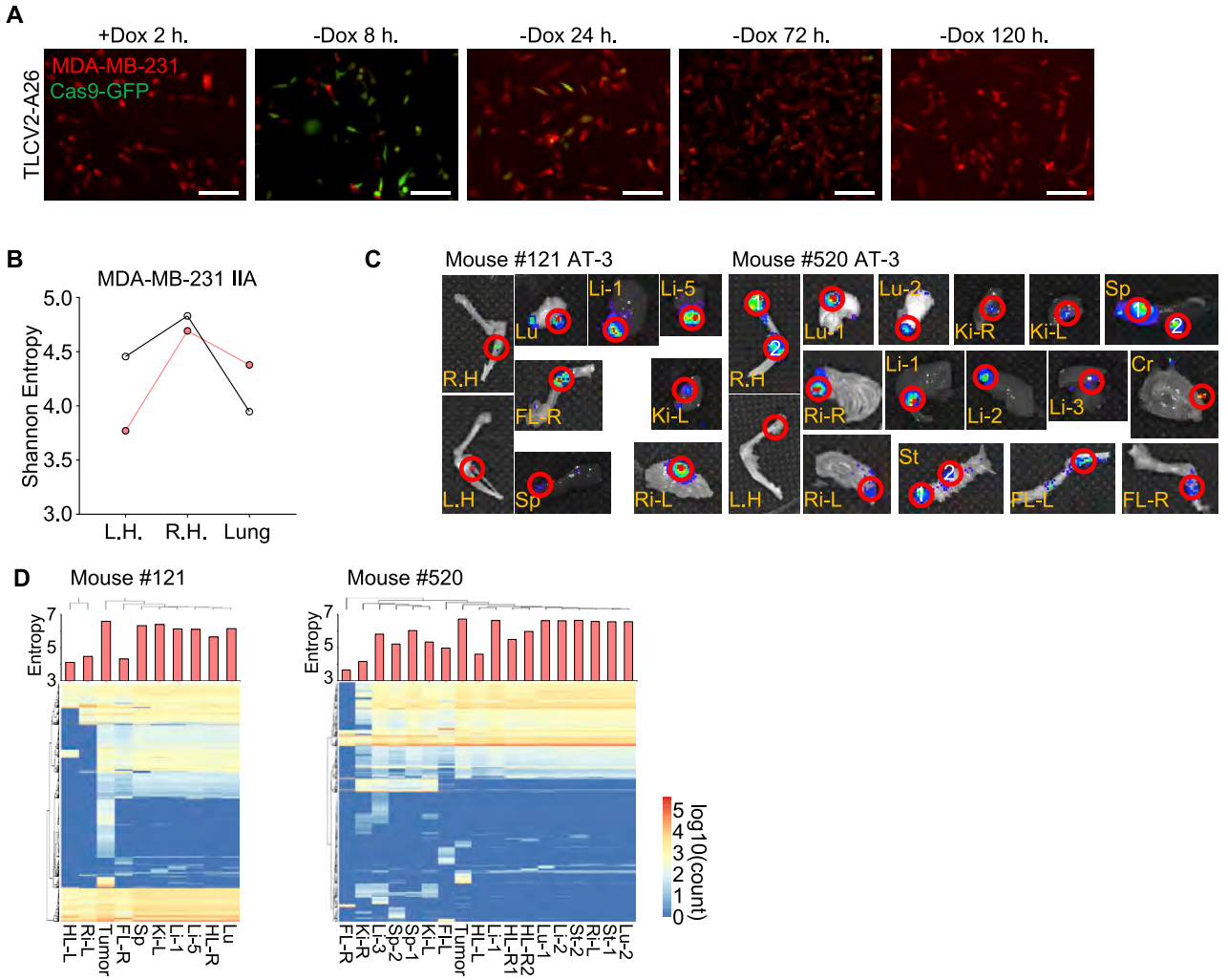

Figure S4. Evolving barcodes in spontaneous metastasis models, related to Figure 4

(A) Fluorescence microscopy showing the expression of EGFP-tagged Cas9 protein in barcoded MDA-MB-231 cells upon a 2-hour doxycycline treatment *in vitro*. Red, cancer cells; Green, Cas9-EGFP. Scale Bar, 100 μm.

(B) Dot plot showing the barcode diversity in samples from right hindlimb (R.H.), left hindlimb (L.H.) and lung of mice received IIA-injected 1E5 barcoded MDA-MB-231 cells at the right hindlimb. Mice were given a dose of 5mg/kg doxycycline via I.P. injection weekly for 5 weeks since 2 weeks after IIA injection. The tissues were collected at week 10.

(C) BLI images of dissected metastatic lesions from C57BL/6J mouse #121 and #520 implanted with AT-3 tumors for barcode analysis.

(D) Feature matrix of mutation events in samples from mouse #121 and #520.

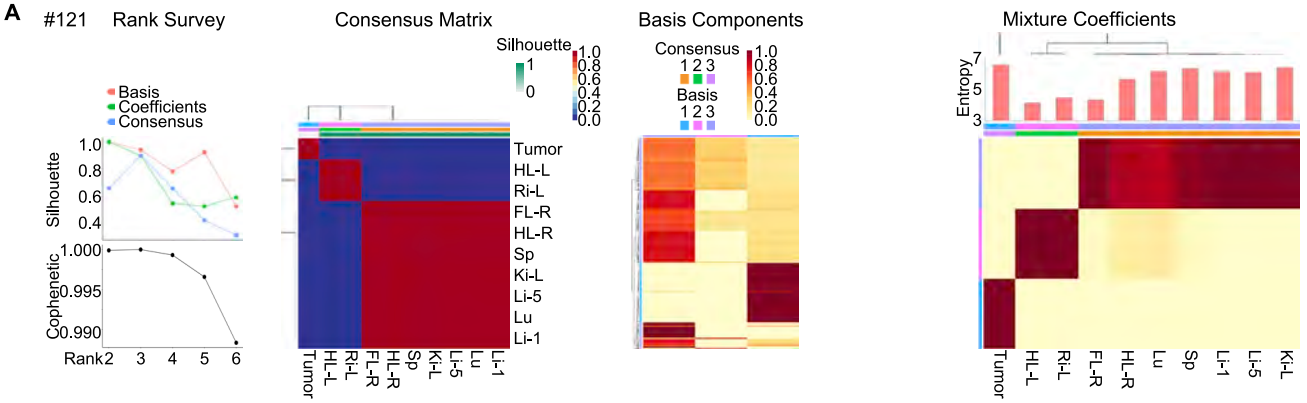

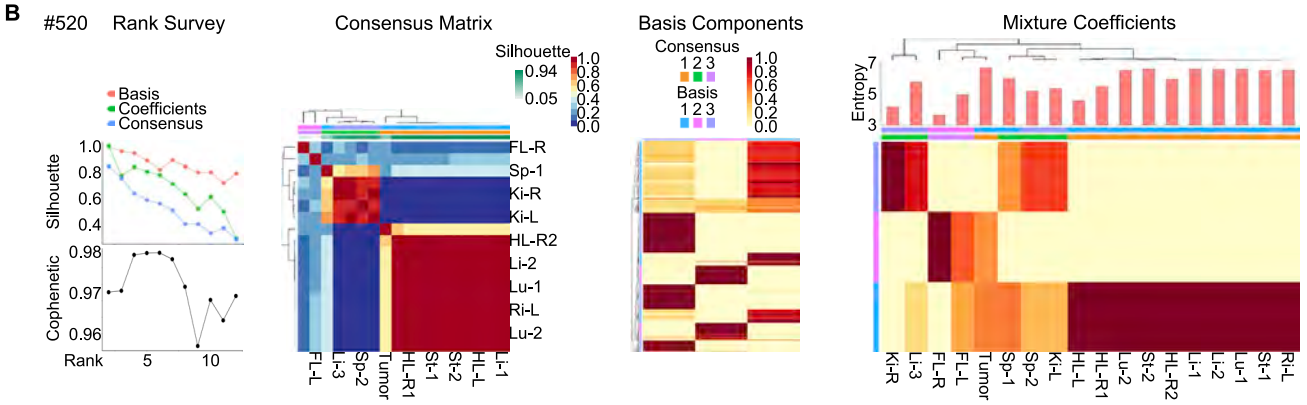

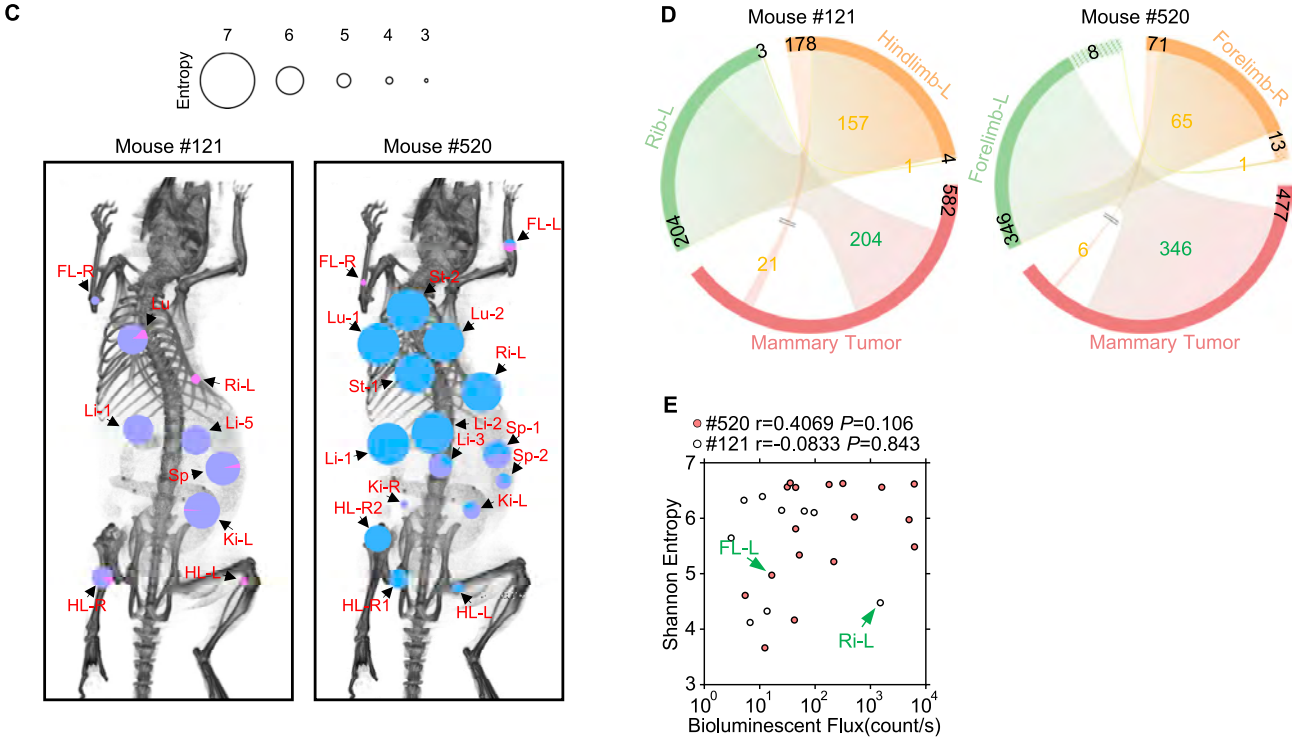

(legend on next page)

Figure S5. NMF analysis of barcoded metastases in syngeneic models, related to Figure 5

(A-B) Plots of NMF rank survey, consensus matrix, basis components matrix and mixture coefficients matrix of 200 NMF runs on the barcodes from metastatic lesions of mouse #121 (A) and #520 (B).

(C) Body maps showing the transformed composition of basis components in AT-3 metastatic lesions.

(D) Chord diagrams illustrating the composition flow of mutation events between primary tumors and selected metastatic lesions in mouse #121 and #520.

(E) Correlation plot of Shannon entropy and metastatic burden of AT-3 lesions. The metastatic burden was determined by BLI intensity. Spearman r and p values were indicated.

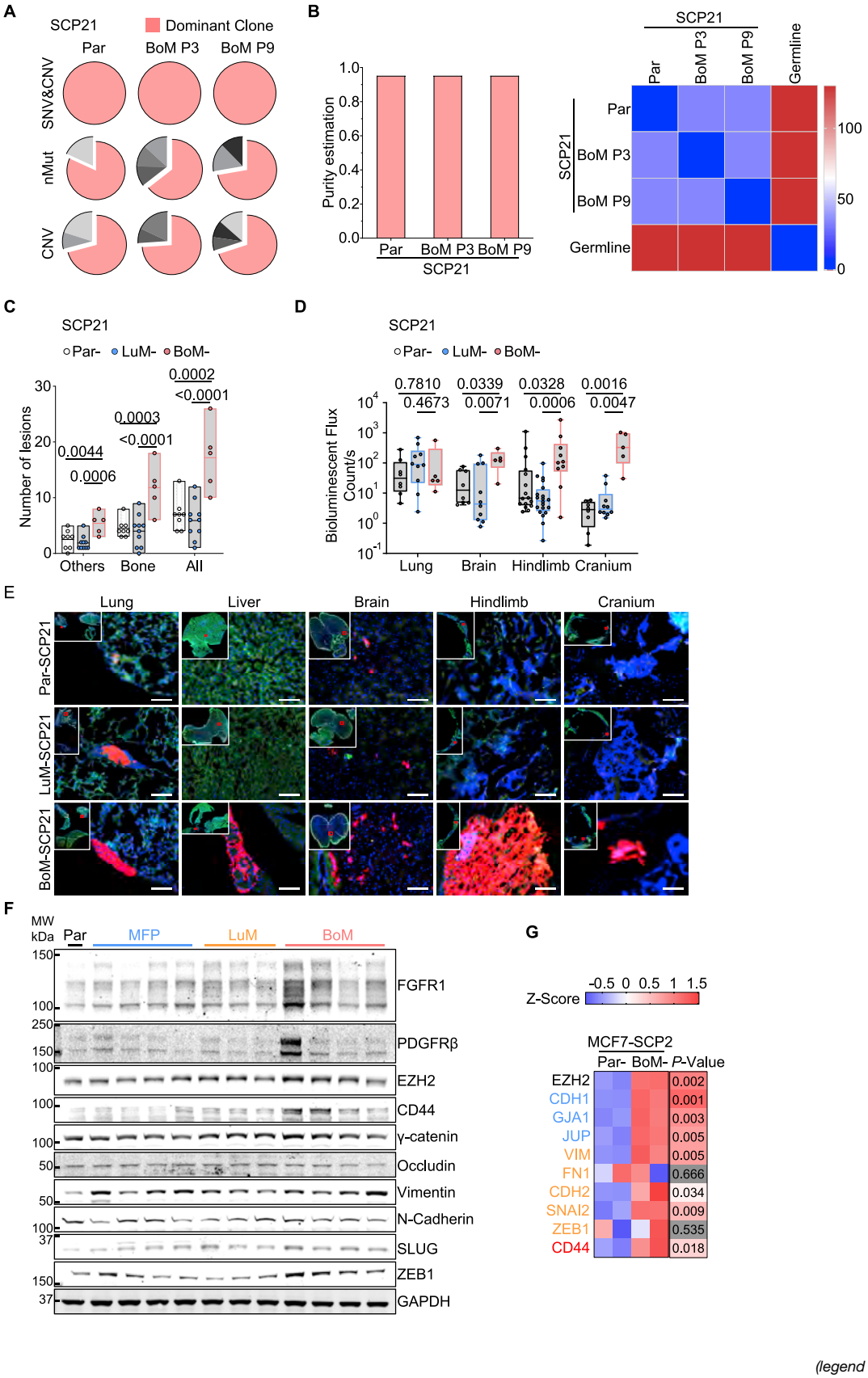

(legend on next page)

Figure S6. Bone-entrained tumor cells are more metastatic and less organo-tropic, related to Figure 6

(A) Pie chart depicting the major clones predicted by EXPANDS package on whole exome sequencing (WES) data of parental, passage 3 and passage 9 bone entrained SCP21 cells.

(B) Histogram (left) depicting the estimated purity and heatmap (right) showing the genetic distance among parental, passage 3 and passage 9 bone entrained SCP21 cells following subpopulation prediction of EXPANDS package. Germline was used as a reference sample.

(C-E) The number of metastatic lesions (C), tumor burden (D) and representative immunofluorescent images (E) in non-bone and bone tissues from mice received IC injection of Par-, LuM-, or BoM-SCP21 cells. Tumor burden on other organs were not compared as few metastases were detected on those tissues. n (# of mice) = 8 (Par); 10 (LuM); 5(BoM). In (E), smaller fields were acquired in tiles by mosaic scanning and then stitched by Zen to obtain complete views of entire organs. Scale bar, 100 μm.

(F) Representative western blotting images in Par-, MFP-, LuM-, and BoM-SCP21 cells.

(G) Relative mRNA levels of selected genes in BoM- and parental MCF7-SCP2 cells. Blue, Epithelial markers; Orange, Mesenchymal markers or EMT promoters; Black, Epigenetic regulators; Red, Stemness markers. The mRNA levels were determined by qRT-PCR, and then transformed into Z-score. n (# of replicate) = 2. *p* values were assessed by Fisher's LSD test following one-way ANOVA test in (C); by Dunn's test following Kruskal-Wallis in (D); by Student's t test in (G).

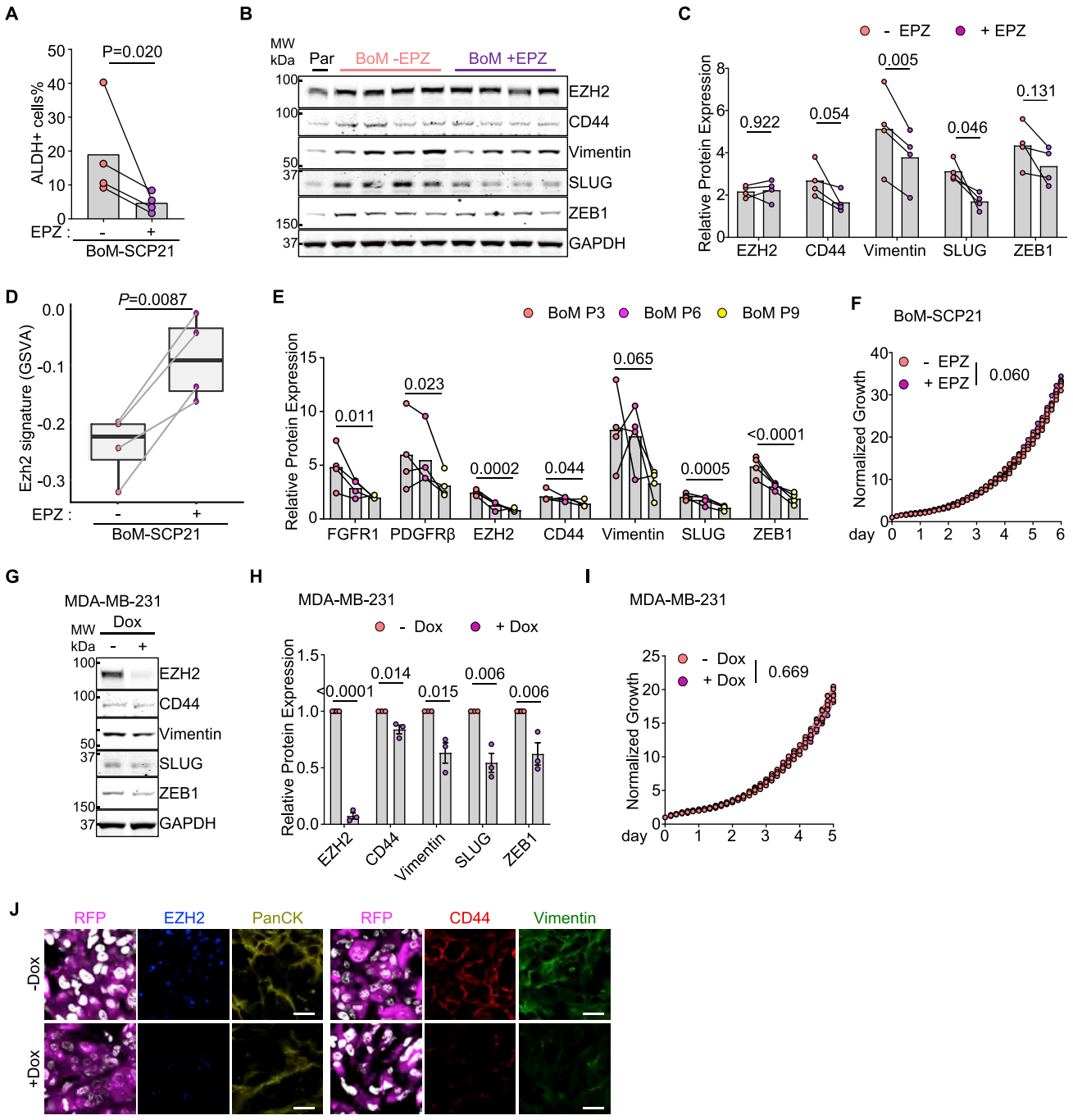

Figure S7. Enhanced spread from bone metastases is mediated by EZH2 activity, related to Figure 7

(A) Bar and dot plot showing the percentage of ALDH1+ population in BoM-SCP21 cells upon 5-day *in vitro* EPZ treatment.

(B-C) Representative western blotting images (B) and quantification (C) in BoM-SCP21 cells upon 5-day *in vitro* EPZ treatment.

(D) Bar and dot plot showing the levels of EZH2 signature in BoM-SCP21 cells upon 5-day *in vitro* EPZ treatment.

(E) Quantification of the protein expression levels in BoM-SCP21 cells at different passages by western blotting.

(F) *In vitro* growth kinetics of BoM-SCP21 cells with or without 1 μM EPZ treatment, shown as the increase of the confluency determined by Incucyte. n (# of replicate) = 4.

(G-H) Representative western blotting images (G) and quantification (H) of proteins in MDA-MB-231 cells after depletion of EZH2 protein. Cells were treated with 1 μg/ml doxycycline to deplete the expression of EZH2 or PBS *in vitro* for 48 hours.

(legend continued on next page)

(I) *In vitro* growth kinetics of MDA-MB-231 cells after knockdown of EZH2. n (# of replicate) = 4.
(J) Confocal imaging of proteins in primary bone lesions of mice received either doxycycline or vehicle. Scale bar, 20 μm.
Data are represented as mean ± SEM in (F), (H) and (I). *p* values were determined by test for linear trend following repeat measure one-way ANOVA in (E); ratio paired t test in (A), (C), and (D); by LSD test following two-way ANOVA in (F) and (I); by Student's t test in (H).